Université du Québec
à Rimouski

RHÉOLOGIE DE LA ZONE MARGINALE DE GLACE : MESURE DE LA VISCOSITÉ DE CISAILLEMENT DE LA GLACE DE MER EN PRÉSENCE DE VAGUES

MÉMOIRE PRÉSENTÉ

dans le cadre du programme de maîtrise en océanographie

en vue de l'obtention du grade de maître ès sciences

PAR

©ÉLOÏSE PELLETIER

Mai 2024

Composition du jury :

Guillaume Boutin, examinateur externe, Nansensenteret, Bergen, Norvège

Dany Dumont, directeur de recherche, Université du Québec à Rimouski

Daniel Bourgault, codirecteur de recherche, Université du Québec à Rimouski

Cédric Chavanne, président du jury, Université du Québec à Rimouski

Dépôt initial le 18 décembre 2023 Dépôt final le 7 mai 2024

UNIVERSITÉ DU QUÉBEC À RIMOUSKI
Service de la bibliothèque

Avertissement

La diffusion de ce mémoire ou de cette thèse se fait dans le respect des droits de son auteur, qui a signé le formulaire *« Autorisation de reproduire et de diffuser un rapport, un mémoire ou une thèse »*. En signant ce formulaire, l'auteur concède à l'Université du Québec à Rimouski une licence non exclusive d'utilisation et de publication de la totalité ou d'une partie importante de son travail de recherche pour des fins pédagogiques et non commerciales. Plus précisément, l'auteur autorise l'Université du Québec à Rimouski à reproduire, diffuser, prêter, distribuer ou vendre des copies de son travail de recherche à des fins non commerciales sur quelque support que ce soit, y compris l'Internet. Cette licence et cette autorisation n'entraînent pas une renonciation de la part de l'auteur à ses droits moraux ni à ses droits de propriété intellectuelle. Sauf entente contraire, l'auteur conserve la liberté de diffuser et de commercialiser ou non ce travail dont il possède un exemplaire.

REMERCIEMENTS

J'aimerais remercier en premier lieu prof. Dany Dumont, mon directeur de maîtrise, pour ses explications simples de sujets complexes, sa patience et sa passion. Merci Dany d'avoir été présent tout au long des défis et des aléas de la vie, et d'avoir partagé ta curiosité sans fin. Merci à prof. Daniel Bourgault, co-directeur de cette maîtrise, pour ses commentaires et sa correction du mémoire. J'aimerais aussi remercier Jérémy Baudry pour l'aide fournie, pour les pépins de codage et les soucis de maths. Merci à Élie Dumas-Lefebvre pour les sessions de pratique de drone et les discussions sur l'art et la vie. Un merci particulier aux frères Guy et Yves Gilbert, des pioniers dans la fabrication et la réparation de canots à glace au Québec qui ont assurés la sécurité des embarcations utilisées lors des campagnes. Merci à mes amis en or, à mes proches et à ceux qui m'ont encouragé sans relâche, qui m'ont permis de prendre un pas de recul, et avec qui j'ai pu relativiser sur les pourquoi et comment des études supérieures.

Merci au Conseil de recherche en sciences et en génies du (CRSNG) Canada pour le financement à travers la subvention à la Découverte détenue par Dany Dumont, ainsi qu'à travers un programme temps navire. Merci à l'Institut des sciences de la mer de Rimouski (ISMER) et prof. Dany Dumont pour le soutien financier. Merci à la Garde côtière canadienne et à Amundsen Science pour l'expédition DarkEdge 2021 dans la Baie de Baffin et surtout, un merci spécial à l'équipage de l'Amundsen d'avoir enrichi cette expérience unique de par leur présence et d'avoir partager leur expertise de navigation dans l'Arctique.

RÉSUMÉ

Mots clés : glace de mer, zone marginale de glace, viscosité, cisaillement, distribution de taille des floes, vagues, rhéologie, atténuation, Arctique

En déployant un aéronef télépiloté (ATP) près de la marge de glace dans l'estuaire du Saint-Laurent, des images aériennes de la propagation oblique de vagues dans la zone marginale de glace (MIZ) ont été obtenues. L'utilisation de la vélocimétrie par images de particules sur une sélection de onze (11) événements filmés a permis de quantifier plusieurs paramètres physiques, tels que la hauteur significative des vagues ($H_s \sim 1$ m), la période moyenne ($T \sim 3 - 4$ s), l'angle d'incidence ($\theta \sim 22 - 48^{\circ}$) et le coefficient d'atténuation de l'énergie des vagues ($\tilde{\alpha} \sim O(10^{-2})$) m^{-1}. Ces données sont utilisées pour contraindre un modèle d'équilibre entre les forces radiatives des vagues et les forces internes de la glace afin d'estimer, pour la première fois à partir d'observations directes, la viscosité de cisaillement ($\eta \sim O(10^3 - 10^4)$) kg s^{-1} de la zone marginale, en supposant celle-ci homogène. Toutefois seulement trois événements permettent d'obtenir une estimation quantitative, alors que les données des huit autres événements suggèrent que la viscosité de cisaillement n'est pas uniforme à travers la MIZ. L'application d'une technique de fenêtrage discret pourrait aider à développer et améliorer le modèle proposé. La comparaison des valeurs obtenues avec deux modèles rhéologiques montre que la MIZ est mieux representée par une rhéologie granulaire de type Mohr-Coulomb que par la rhéologie visco-plastique qui est la plus largement utilisée dans les modèles de glace.

ABSTRACT

Keywords : sea ice, marginal ice zone, viscosity, shear, floe size distribution, waves, rheology, attenuation, Arctic

By deploying unmanned aerial vehicle (UAV) at the ice edge in the St. Lawrence Estuary, we obtained aerial footage of oblique wave propagation in the marginal ice zone (MIZ). Applying particle image velocimetry to a selection of eleven (11) video sequences allowed quantifying numerous dynamical parameters such as the significant wave height ($H_s \leq 1$ m), mean period ($T \simeq 3-4$ s), angle of incidence ($\theta \simeq 22-48^\circ$) and wave energy attenuation coefficient ($\tilde{\alpha} \sim O(10^{-2})$) m^{-1}. An equilibrium model was developed and applied to estimate the shear viscosity ($\eta \sim O(10^3-10^4)$) kg s^{-1} for three events. The application of the model on the eight (8) other events suggests that the shear viscosity might not be constant through the MIZ and that a discrete windowing technique could help develop and ameliorate the model. Comparing estimated shear viscosity values to two rheologies showed that the MIZ behavior is best represented by the Mohr-Coulomb granular theory over the widely used Hibler's viscous-plastic rheology.

TABLE DES MATIÈRES

REMERCIEMENTS v

RÉSUMÉ vi

ABSTRACT vii

TABLE DES MATIÈRES viii

LISTE DES TABLEAUX ix

LISTE DES FIGURES x

LISTE DES ABRÉVIATIONS xii

INTRODUCTION GÉNÉRALE 1

ARTICLE 1
RHÉOLOGIE DE LA ZONE MARGINALE DE GLACE:
MESURE DE LA VISCOSITÉ DE CISAILLEMENT DE LA GLACE DE MER
EN PRÉSENCE DE VAGUES 19

1.1 Introduction 20

1.2 Conceptual framework 26

1.2.1 Equilibrium momentum equations for an idealized MIZ 27

1.2.2 Parameters and variables 34

1.3 Methods 35

1.3.1 Study site and environmental conditions 37

1.4 Results 38

1.4.1 Ice conditions 38

1.4.2 Dynamical quantities derived from the ice velocity field 43

1.4.3 Shear viscosity 55

1.5 Discussion 58

1.6 Conclusion 64

CONCLUSION GÉNÉRALE 66

RÉFÉRENCES 68

LISTE DES TABLEAUX

1 Variables and parameters used in this document. 34

2 UAV flight and photogrammetric data. 39

3 Estimates of relevant physical quantities for the selected events. The first column represents the space and time average velocity, θ is the angle of incidence of the waves, $\overline{H_s}$ is the mean significant wave height, $\overline{T}$ the mean wave period, $\left\langle \frac{\partial E}{\partial x} \right\rangle$ is the wave energy attenuation along the x-axis, $\tilde{\alpha}$ and α are the wave energy attenuation coefficients along the x-axis and along the direction of propagation, respectively, $\frac{\partial^2 v}{\partial x^2}$ is the second-order derivative of the mean along-edge velocity, $|\dot{\varepsilon}_{12}|$ is the deformation rate (shear rate) module and finally $\langle \eta \rangle$ is the mean shear viscosity. 49

LISTE DES FIGURES

1 Canot à glace déployé dans la MIZ, vu d'un drone. On y voit 5 membres de l'équipage et des instruments de mesures, tel un ADCP (Acoustic Doppler Current Profiler) pour quantifier les fluctuations de vitesse, près de Saint-Fabien-sur-mer, Québec, Canada, le 12 février 2020. On peut aussi y observer la diversité de topographie, d'épaisseur et de taille des différents *floes* présents. 15

2 Image satellite de Saint-Fabien-sur-mer et ses environs, Québec, Canada, le 8 juillet 2023 à 15 : 39 : 49UTC. Source : Sentinel-2, Agence spatiale européenne (ESA). 16

3 Schéma méthodologique détaillant les différentes étapes de conceptualisation, acquisition des données et traitement subséquent jusqu'à l'application finale du modèle développé pour la viscosité de cisaillement. 18

4 Aerial picture of the marginal ice zone off Anse-à-Mercier, Saint-Fabien-sur-mer, Québec, Canada on March 7, 2019, 16:37 EDT. Air temperature is $T_{\text{air}} \simeq -11°\text{C}$ and the wind is blowing from the west ($\sim 270°$) at 30 km h^{-1}, according to the Environment Canada weather station of Pointe-au-Père. The ice edge is highlighted by the white band. Waves are progressively attenuated as they propagate in the MIZ, with short waves being attenuated more rapidly than longer waves. 27

5 Schematic top view representation of a stationary marginal ice zone hit by surface gravity waves. The main coordinate system is described by (x, y), with the axis respectively perpendicular and parallel to the edge. (x', y') refer to a rotation of this system in order to be aligned with the direction of wave propagation. θ is the angle of incidence of the waves and $x = 0$ delimits the ice edge. 31

6 Location of all 11 events overlaid on bathymetric data. 33

7 Total wave energy distribution in the MIZ for $E_0 = 0.1$ m^2 and $\alpha = 2.6 \times 10^{-2}$ m^{-1}, pertaining to different incidence angle θ. 37

8 Ice conditions for all eleven (11) events in chronological order, with UTC date and time. Images are oriented so that the ice edge is on the left with waves coming in from the lower left corner. 40

9 Larger-scale ice conditions for February 20 and 24, 2022, depicting the heterogeneity of the ice cover for events #6, #7 and #11. 42

10 Spatial distribution of the temporal mean along-edge velocity $\overline{\mathbf{v}}(x, y)$ in m s^{-1} for event #1 and #6. In (a), the mean velocity is decreasing following a second-order polynomial fit, with the shape of an inverted parabola. The total mean velocity (through all frames and in x and y) is 0.65 m s^{-1}. In (b), the mean along-edge velocity is decreasing following an exponential. The total mean velocity is 0.14 m s^{-1}. 44

11 Temporal variation of the v-component of the orbital velocity for the video duration, in m s^{-1}. 45

12 Spatial distribution of the v-component of the orbital velocity in m s^{-1} (colorscale) for the first frame, with the geometric decomposition of the angle of incidence θ, for event #1. 46

13 Averaged shape of the amplitude variance spectrum for event #6, for frequencies between 0.2 and 0.5 Hz. 47

14 Spatial distribution of the total wave amplitude variance $E(x, y)$ (colorscale), superimposed with the along-edge average $E(x)$ (black line) and the exponential fit (red line), in m^2, for event #6. 48

15 Comparison of spatial distributions of total amplitude variance for event #3 and #4: the patchy detection of amplitude in the water (40 first meters of event #3) is similar to the mix of new ice (20 first meters of event #4). 52

16 Spatial distributions of the along-edge velocity $\overline{v}$ and of the total wave amplitude variance $E(x, y)$ (colorscale), superimposed with the along-edge averages (black line) and respective polynomial and exponential fits (red line) for 2 selected events (#7, 10). 53

17 Spatial distribution of the temporal mean along-edge velocity $\overline{v}$ in m s^{-1} for event #3, where we see an upward trend with distance to the edge. 54

18 Shear viscosity values estimated using equation 1.15 for events #6, #7 and #10 (red dots from left to right) superimposed with the prediction of the viscous-plastic rheology of Hibler (1979) (H79, black) and the Mohr-Coulomb rheology of Uzuner and Kennedy (1976) (UK76, yellow) for a range of possible parameter values ($h = [0.2, 0.8]$ m, $e = 2.0$, $P^* = 2.75 \times 10^4$ Pa, $n = [0.3, 0.5]$ and $\phi = [26, 58]^\circ$. 57

19 Shear viscosity variation for event #10. The black curve represents the variation of η along the x-axis, while the three other curves have been obtained and calculated for three windows on the image: window 1 covers the first 80 m, window 2 is for $x \in [81, 161]$ m and window 3 for $x \in [162, 242]$ m. . . 60

LISTE DES ABRÉVIATIONS

ADCP Acoustic Doppler Current Profiler

ATP Aéronef télépiloté

BdHH Baie du Ha ! Ha !

CEAREX Coordinated Eastern Arctic Experiment

CIS Canadian Ice Service

EB Elasto-Brittle

ESA European Spatial Agency

EVP Elasto-visco-plastic

FFT Fast Fourier Transform

FSD Floe Size Distribution

GPS Global Positioning System

GUI Graphical User Interface

LIMEX Labrador Ice Margin Experiment

MIZ Zone marginale de glace (*Marginal Ice Zone*)

MIZEX Marginal Ice Zone Experiment

NOAA National Oceanic and Atmospheric Administration

NSIDC National Snow and Ice Data Center

PIV Particle Image Velocimetry

RSTA Royal Society Transactions A

SIE Sea ice extent

SIT Sea ice thickness

SIZEX Seasonal Ice Zone Experiment

UAV Unmanned Aerial Vehicle

VP Visco-plastic

WMO World Meteorological Organization

WRS Wave radiative stress

INTRODUCTION GÉNÉRALE

Selon le rapport sur le climat global produit par NOAA en octobre 2023 (NOAA-NCEI, 2023), l'année 2023 possède une probabilité de plus de 99 % d'être l'année la plus chaude jamais enregistrée, une représentation inquiétante du réchauffement planétaire. Alors que les températures mondiales ne cessent d'augmenter, l'Arctique connaît un taux de réchauffement près de quatre fois plus élevé que le reste de la planète (Rantanen et al., 2022). De nombreuses études ont mis en évidence une diminution de l'étendue de la glace de mer (Stroeve et al., 2014; Cavalieri and Parkinson, 2012; Meier et al., 2005) et de l'épaisseur de la glace de mer (Kwok and Rothrock, 2009) en relation avec ce réchauffement. Les données des dernières années démontrent non seulement une diminution générale de la glace, mais aussi une accélération dans la tendance. Entre 1998 et 2008, le déclin décennal de l'étendue de la banquise arctique (saisonnière et pérenne) a atteint -10.1% à -10.7% par rapport à -2.2% à 3.0% entre 1979 et 1996 (Comiso et al., 2008). Depuis les années 2000, de nouveaux records d'étendue minimale de glace pour l'Arctique se succèdent : en 2007, ce minimum était de 4.1 millions km^2 (Comiso et al., 2008) remplacé 5 ans plus tard, en 2012, par un record de 3.41 millions km^2 (NSIDC, 2012).

La disparition, même partielle, de la couverture estivale de glace dans l'Arctique pourrait mener à une cascade d'effets sur le climat mondial, étant donné le rôle crucial des banquises polaires dans la circulation générale. Un retrait de la glace de mer, avec son couvert blanc de neige et sa surface claire, expose une plus grande surface foncée d'eau libre qui absorbe fortement la radiation solaire et mène à une augmentation de la température de surface des océans (Haas et al., 2005). Cette hausse de température encourage à son tour la fonte du couvert glaciaire et entraîne un cycle de fragilisation de la glace. Ce nouveau taux de fonte et le changement associé dans la saisonnalité de la glace arctique (Strong and Rigor, 2013) amènent une superficie d'eau libre élargie et subséquemment un amincissement et un découvrement de la glace de mer (Cavalieri and Parkinson, 2012). La diminution en concentration

entraîne également une augmentation du *fetch* du vent et conséquemment de l'énergie mécanique des vagues de surface (Thomson and Rogers, 2014). L'exposition accrue de la banquise aux vagues de plus grande amplitude et de plus basse fréquence contribue significativement à sa fragmentation, activant ainsi des boucles de rétroactions, négatives et positives, pouvant affecter l'évolution subséquente du couvert de glace et du climat. Dans ses travaux récents, Kim et al. (2023) quantifie la perspective d'un futur où l'Arctique se retrouverait libre de glace en été (étendue inférieure à 1×10^6 km^2) et prédit la possibilité de cette occurrence d'ici le milieu du siècle. Ces récentes prévisions soulignent l'urgence d'améliorer les modèles de glace afin d'anticiper et de caractériser les changements considérables à venir et leurs effets sur l'atmosphère et l'océan.

Cette diminution de glace de mer arctique en été entraîne un autre changement significatif : la transition de la glace pérenne à la glace saisonnière (Polyakov et al., 2012). Dans les années 1980, la glace âgée de plus de 4 ans représentait jusqu'à plus du tiers de la composition de la banquise arctique. Selon les travaux de Perovich et al. (2021), cette fraction a considérablement diminué pour atteindre environ 4.4% en 2020. Comiso et al. (2017) caractérise aussi ce déclin drastique et confirme, en analysant quatre produits de données satellitaires sur la glace de mer, que le taux de déclin de l'étendue de glace arctique pérenne est de 11% par décennie. Kwok (2018) constate qu'au cours de la période 1999-2017, l'Arctique a perdu plus de 50% de sa glace pluriannuelle (plus de 2 ans). Cette étude documente également, pour le centre de l'Arctique, une diminution de la moyenne estivale d'épaisseur de 60% sur six décennies. Alors qu'un déclin drastique est observé en été, la diminution de la glace de mer affecte l'Arctique en toutes saisons, comme l'ont démontré Meier et al. (2014), Serreze et al. (2007) et bien d'autres. En outre, de récentes recherches menées par Belter et al. (2020) révèlent que l'épaisseur modale de la glace a diminué de plus de 20% entre 2001 et 2020.

Cette glace plus jeune, survivant de moins en moins à la fonte estivale, devient précaire et susceptible d'être fragmentée, et même détruite, par des évènements de tempête. Comme mentionné précédemment, cette fragilisation et le déclin qu'elle entraîne rendent disponible

davantage d'énergie pour la croissance des vagues, ce qui entraîne l'émergence d'un climat fortement contrôlé par celles-ci pour l'Arctique (Thomson and Rogers, 2014). Documenté au cours des 20 dernières années, ce phénomène a entraîné une réduction de l'étendue de la glace de mer, une augmentation de la hauteur et de la longueur d'onde des vagues, ainsi que des houles plus persistantes (Stopa et al., 2016). Ces vagues plus énergétiques contribuent à une fragmentation accrue de la banquise (Asplin et al., 2012), se traduisant par une distribution de taille des *floes* plus fine. Une diminution de la grosseur des *floes* entraîne une fonte et une dérive plus rapides (Squire, 2007), permettant et favorisant une pénétration accrue des vagues dans le couvert de glace (Emmanuel et al., 2022). Ces vagues d'énergie supérieure pourraient devenir plus fréquentes, si les prévisions de hausse des conditions de tempête pour l'Arctique s'avèrent exactes (Day and Hodges, 2018; Khon et al., 2014).

La zone marginale de glace (*Marginal Ice Zone*, MIZ) est une zone d'interactions entre l'océan libre et la glace. La concentration de glace de mer (*Sea Ice Concentration, SIC*) est la caractéristique la plus facile à détecter et peut être utilisée pour définir de manière plus tangible la MIZ [e.g.(Vichi, 2021)]. Elle est dérivée à grande échelle à partir de données satellitaires, notamment grâce aux capteurs à micro-ondes passifs. La définition la plus largement utilisée de la MIZ est la zone de l'océan couvert de glace adjacente à une portion de l'océan libre de glace où la concentration est comprise entre 15% et 80%. Bien que cette définition puisse être appropriée dans certains contextes spécifiques, les MIZ observées et décrites dans le présent mémoire possèdent des concentrations élevées (entre 95-100%). Cette étude étant centrée sur l'interaction vagues-glace, la définition pour laquelle nous optons exclus des critères de concentration. Nous utilisons plutôt une définition impliquant l'influence des vagues sur la glace. Dans cette étude, nous définissons donc la MIZ comme étant la région où la couverture de glace est affectée par les vagues générées par le vent dans la portion de l'océan qui y est adjacente. Cette définition est similaire à celle d'autres études s'étant intéressées aux interactions vagues-banquise (Squire, 2020; Wadhams et al., 1986). Entres autres, la revue de Dumont (2022) présente et détaille plus en profondeur différentes définitions qui chacune évoque un ou plusieurs aspects et comportement de la MIZ.

Aux vagues de gravité, comme à plusieurs types d'ondes, est associé un flux de quantité de mouvement. Lorsque ce flux varie dans l'espace, il produit un excès exerçant une force sur le milieu (Longuet-Higgins and Stewart, 1964). Étant donné que la glace atténue les vagues, générant ainsi une variation spatiale de quantité de mouvement, celles-ci lui imposent en retour une force significative, un processus connu sous le nom de contrainte ou pression de radiation. Cette force est donc particulièrement importante à la lisière de la glace (Dai et al., 2019), à la jonction entre l'eau libre et la banquise, là où l'énergie des vagues est la plus grande et où l'atténuation y est la plus importante. Sutherland and Dumont (2018) ont montré à partir d'observations dans la zone marginale du Parc National du Bic, près de Rimouski, combinées à un modèle simple, que la contrainte radiative peut surpasser de plusieurs ordres de grandeurs les forces dues au vent et au courant, en plus de mener à un épaississement significatif de la banquise et à la génération de courant *jet* près de la marge. Ils ont ainsi démontré que la contrainte radiative ne peut pas être ignorée si l'on souhaite bien représenter la dynamique de la MIZ. Dans la banquise périphérique de l'océan Austral, cette contrainte est dominante (Stopa et al., 2018) et des hypothèses ont été émises selon lesquelles elle pourrait devenir de plus en plus importante dans l'Arctique également (Boutin et al., 2020). Squire (2020) abonde dans ce sens et suggère qu'avec le réchauffement accéléré de l'Arctique, la banquise estivale pourrait commencer à adopter un comportement ressemblant à celui de la glace de mer en Antarctique.

En combinant l'augmentation de l'énergie disponible à la génération de vagues à la définition de la MIZ, on peut prédire que l'échelle spatiale de cette zone augmentera et que, par conséquent, sa compréhension devient de plus en plus importante pour prédire l'avenir de la glace de mer dans l'Arctique. Cette hypothèse est renforcée par Aksenov et al. (2017) qui déclare que l'intensification de l'étendue de la MIZ est à prévoir, ainsi que par Boutin et al. (2020) suggérant que les interactions vagues-glace pourraient être un des facteurs dominants de son évolution.

Malgré la littérature existante concernant la dynamique de la MIZ, certains aspects

restent encore à élucider et à modéliser. Pour être pleinement intégrée dans les modèles, la propagation des vagues dans les eaux couvertes de glace doit continuer à être étayée, car elle a été jusqu'à maintenant principalement étudiée de manière théorique. Squire (1995, 2007, 2020) a produit une série de revues sur les interactions entre les vagues et la glace montrant la complexité des processus coexistants dans ces interactions. Cheng et al. (2020) indique également que toutes ces ramifications n'ont pas encore été pleinement intégrées dans les modèles.

L'omission de ces interactions est susceptible de conduire à des simulations numériques moins précises, car la paramétrisation des tempêtes, des vents et des vagues représentent toujours un défi (Stroeve et al., 2014). L'écart entre les résultats des modèles et les observations montre la nécessité d'une meilleure paramétrisation de la propagation des vagues à travers la glace (Squire, 2018). Plusieurs études (Tietsche et al., 2014; Comiso et al., 2017) ont montré que la région présentant les erreurs les plus importantes dans les modèles de glace de mer est la zone marginale. Au cours de la dernière décennie, une émergence sans précédent sur les études concernant sa dynamique a pris place, réitérant à multiples reprises la pertinence d'une meilleure compréhension des interactions entre les vagues et la glace. L'une des limitations ressortant de cette documentation et ayant trait à la quantification de la MIZ est la rareté d'observations in situ (Ardhuin et al., 2015).

En effet, la zone marginale est difficilement accessible. La forte concentration de glace empêche la plupart des navires de naviguer à l'intérieur sans perturber le champ de glace et le manque de consolidation entre les *floes*, souvent en forme de crêpes et glaçons près de la marge, rend les déplacements à pied périlleux. Quelques campagnes ont eu lieu dans les années 80 et 90, *The Marginal Ice Zone EXperiment* (MIZEX) étant le premier projet d'exploration sur le terrain dans la MIZ de l'océan Arctique (Johannessen, 1987). Les campagnes MIZEX ont commencé en 1983 et ont continué jusqu'en mars et avril 1987 dans le détroit de Fram. L'objectif principal était d'améliorer la compréhension des processus physiques à méso-échelle régissant les interactions glace-océan-atmosphère et d'en déterminer

les termes dominants dictant le mouvement de la glace. Des efforts complémentaires, tels que l'étude de l'activité biologique et du bruit ambiant à la lisière (Rottier, 1989), furent aussi déployés. Ces campagnes ont étés suivies par plusieurs autres, tel que *The Coordinated Eastern ARctic EXperiment* (CEAREX) (Group, 1990), examinant plus particulièrement l'échange de quantité de mouvement, de chaleur et de biomasse, ainsi que le comportement de la glace et le bruit ambiant acoustique, faisant ainsi suite aux objectifs de MIZEX. On note aussi *The Seasonal Ice Zone EXperiment* (SIZEX) (Johannessen et al., 1990) dans le détroit de Fram et, se concentrant sur la propagation des vagues dans la MIZ dans la mer du Labrador, *The Labrador Ice Margin EXperiment* (LIMEX) (Liu et al., 1991).

Ces ensembles de données in situ, bien que fondamentaux, ont été échantillonnés dans des conditions de glace limitées. Malgré l'apparition de la télédétection, constituant un outil considérable dans l'obtention de données polaires, Cooper et al. (2022) affirme que les plus récentes base de données de produits satellitaires ne sont pas encore extensives et/ou accessibles, même en considérant leur progression récente (entres autres par Stopa et al. (2018) et Brouwer et al. (2022)). L'utilisation d'aéronefs télépilotés (ATP) facilite grandement l'accès aux environnements de terrain dangereux, tels que les crevasses des glaciers (Chudley et al., 2019) et la MIZ (Dumas-Lefebvre and Dumont, 2023).

Malgré la constance de l'engagement de la communauté scientifique sur le sujet, le besoin d'études sur le terrain quantifiant simultanément la propagation et l'atténuation des vagues dans les eaux couvertes de glace est toujours présent. Pour une incursion plus profonde dans l'état des connaissances et dans les pistes de recherche, les articles du numéro spécial intitulé *Theory, modelling and observations of marginal ice zone dynamics : multidisciplinary perspectives and outlooks* de la revue Philosophical Transcastions of the Royal Society A, sont conseillés, notamment ceux de Bennetts et al. (2022), Dumont (2022) et Squire (2022).

L'une des caractéristiques les plus notoires de la zone marginale est le fait que la banquise y est généralement composée de *floes* (morceaux) de petite taille en comparaison avec la banquise intérieure. Les vagues peuvent parcourir des centaines de kilomètres dans la MIZ

[e.g. Dumont et al. (2011); Kohout et al. (2014)], tout en fractionnant les *floes* en morceaux dont la taille dépend des propriétés mécaniques de la glace et des caractéristiques des vagues. Lorsqu'agités, les *floes* fragmentés peuvent être compactés, empilés et/ou érodés. De manière générale, la MIZ peut comporter à la fois des zones de production et de consolidation de la glace, peut contenir des chenaux, des fractures ou se trouver aux abords d'une polynie. Le chevauchement et la formation de crêtes ne sont pas rares, et les conditions hautement dynamiques favorisent les échanges thermodynamiques ainsi que les interactions entre l'océan, la glace et l'atmosphère. Malgré une composition variable, elle est principalement constituée de jeune glace, qu'il s'agisse de nouvelle glace, de sarrasins, de nilas ou de glace en crêpes.

Dans le cadre de ce mémoire, nous portons une attention particulière à la façon avec laquelle la banquise, en tant que matériau, répond au forçage provenant des vagues. La réponse dépend de sa rhéologie, soit la relation entre les contraintes et les déformations, et qui elle-même est sensible à la taille des *floes* et à l'épaisseur. Très peu étudiée de façon expérimentale en milieu naturel, la rhéologie est pourtant une composante fondamentale des modèles numériques climatiques et des systèmes de prévision environnementaux, et ce depuis les travaux pionniers de Hibler (1979). Les paramètres rhéologiques de la banquise sont souvent estimés à partir d'observations de déformations à large échelle (Tremblay and Hakakian, 2006; Bouchat and Tremblay, 2017), principalement dans la région intérieure de l'océan Arctique, mais très peu dans la zone marginale.

Un de ces paramètres est la viscosité, qui peut être définie en fonction de différents processus. La viscosité dite turbulente (*eddy viscosity*) fait référence à la formation de tourbillons sous une couche de glace due à la friction à l'interface. La viscosité normale (*bulk viscosity*) est paramétrée pour des conditions normales, soit en compression. La viscosité de cisaillement est, trivialement, utilisée lors de conditions en cisaillement. Selon son interprétation, elle peut également prendre en compte les interactions entre les *floes* (collisions), les contraintes internes (flexion) et les déformations associées à ces processus (Doble et al., 2015). La viscosité est donc un paramètre permettant de quantifier la réaction d'un matériau

à un forçage.

La quantification de la réponse de la contrainte interne face à un taux de déformation, via ces paramètres rhéologiques, est susceptible d'avoir un impact sur la façon dont la glace de mer est modélisée. Boutin et al. (2023) cite les travaux de Steele et al. (1997) pour expliquer que le transport net de la glace de mer est déterminé par la paramétrisation de la contrainte interne et des termes rhéologiques présents dans la conservation de la quantité de mouvement. Le choix de la rhéologie à appliquer est important pour obtenir une prédiction précise du comportement de la glace de mer. La rhéologie la plus largement utilisée dans les modèles climatiques mondiaux et les modèles glace-océan à grande échelle est la rhéologie visco-plastique dérivée des travaux d'Hibler (1979). La rhéologie élastique-visco-plastique, documentée par Hunke and Dukowicz (1997) et modifiée par Lemieux et al. (2012), est aussi souvent paramétrée dans les solutions numériques. La rhéologie *elasto-brittle* (EB), introduite plus récemment et qui conçoit la glace comme un matériau friable (Bouillon and Rampal, 2015), met l'emphase sur la modélisation des fractures. La rhéologie granulaire, traditionnellement associée au critère de rupture de Mohr-Coulomb (Ip et al., 1990; Dai et al., 2004), a été également abordée par plusieurs (Shen et al., 1987; Feltham, 2005) et est aujourd'hui considérée comme un modèle prometteur pour une meilleure représentation de la dynamique de la zone marginale (Herman, 2022), principalement car elle propose une résolution des interactions entre les floes.

Dans la rhéologie d'Hibler (1979), le critère de rupture, qui prend la forme d'une surface elliptique dans l'espace des contraintes principales, est fondé sur l'hypothèse que la glace de mer soumise à des conditions de compression ou de cisaillement réagit comme un matériau plastique, c'est-à-dire que les contraintes sont proportionnelles aux déformations. Cette représentation est en fait une application particulière du formalisme de Reiner-Rivlin pour les fluides non-Newtoniens. Si cette rhéologie peut raisonnablement reproduire la dérive et l'épaisseur moyennes de la glace, comme l'a montré Zhang and Hunke (2001), les modèles numériques de glace ne sont pas encore adéquats pour des déformations à petite échelle, et

donc peu adaptés à la MIZ. Kwok et al. (2008) souligne cette affirmation et met en avant la nécessité d'observations à haute résolution de la dérive de la glace.

En 2018, Sutherland and Dumont (2018) ont posé les bases de cette thèse en utilisant la radiation des vagues pour estimer la force de compression, dans le laboratoire naturel que constitue l'estuaire du Saint-Laurent. L'équilibre des contraintes internes est fondé sur la rhéologie granulaire de Mohr-Coulomb et permet de dériver une loi prédictive pour l'épaisseur de la glace, en plus de proposer une nouvelle définition de l'étendue de la MIZ. En s'appuyant sur les travaux fondateurs de Longuet-Higgins and Stewart (1964) et Uzuner and Kennedy (1976), un modèle a été validé et testé pour l'incidence normale des vagues, mais n'a pas couvert le cas d'une incidence oblique conduisant à des conditions de cisaillement. Par conséquent, le projet présenté dans ce mémoire est basé sur les travaux d'Hibler (1979), Hunke and Dukowicz (1997), Longuet-Higgins and Stewart (1964) et Dai et al. (2004), et la méthodologie s'appuie principalement sur les travaux de Sutherland and Dumont (2018) réalisé dans le cadre du programme BicWin.

Les modèles dynamiques de la banquise reposent sur le choix et la formulation d'une rhéologie particulière, décrivant de manière spécifique les paramètres dynamiques reliant les contraintes aux déformations. La présente étude propose une détermination purement empirique de la viscosité de la MIZ à partir de la formulation générale pour les fluides de type Reiner-Rivlin, sans supposer de modèle spécifique pour la viscosité. L'espoir est d'arriver, à l'aide d'observations directes, à informer une forme fonctionnelle spécifique applicable à un modèle dynamique. Pour accomplir cet objectif, nous utilisons des méthodes d'imagerie et de photogrammétrie aérienne afin de quantifier simultanément les contraintes et les déformations, à partir desquelles nous pourrons dériver des valeurs de viscosité. C'est en déployant un ATP (communément appelé drone) au-dessus de la lisière de la zone marginale en présence de vagues près de la côte de Saint-Fabien-sur-mer, Québec, Canada, que nous visons à quantifier la viscosité de cisaillement pour de multiples événements. Les événements que nous documentons ici ont eu lieu à divers moments au cours des hivers 2019 à 2022. Nous

décrirons subséquemment la méthodologie développée pour quantifier simultanément la déformation près de la lisière de la glace et la contrainte radiative provenant du train de vagues à incidence oblique. Ce faisant, nous espérons démontrer que la méthode présentée dans cette étude trouve son originalité non seulement dans la mesure simultanée du champ de vitesse et du taux de déformation, mais aussi dans le développement et la formulation mathématique d'un modèle d'équilibre simple pouvant être appliquée de manière plus générale à d'autres événements.

Objectifs

L'**objectif général** de ce projet de maîtrise est de mieux comprendre et modéliser la physique et la dynamique de la zone marginale de glace. En s'appuyant sur un cadre conceptuel simplifié par les conditions spécifiques de la zone de recherche choisie, nous souhaitons plus particulièrement mieux comprendre la relation entre les contraintes radiatives dues aux vagues et la déformation de cisaillement associée. Les **objectifs spécifiques** sont :

1. Mesurer simultanément la contrainte radiative due aux vagues ainsi que la déformation de cisaillement de la banquise compacte près de la marge.
2. Estimer, à partir de ces observations, la viscosité de la zone marginale sous différentes conditions de glace.

Ces objectifs s'appuient sur le développement d'un cadre conceptuel qui conçoit la glace comme un continuum bidimensionnel de type Reiner-Rivlin. La section suivante explique brièvement les hypothèses et équations principales ayant mené au développement mathématique du modèle présenté et décrit en détail au chapitre 1.

Aperçu du cadre conceptuel

Dans le cadre de l'évaluation des conditions de la zone marginale, nous supposons des situations où les conditions océaniques et atmosphériques varient peu ou lentement. Nous

considérons des phénomènes se déroulant à des échelles de temps et d'espace propres à la propagation des vagues, étant ainsi plutôt courtes par rapport aux échelles de temps associées aux échanges de chaleur. En ce sens, les effets thermodynamiques menant à l'évolution de la banquise sont négligés, tout en reconnaissant que ceux-ci restent déterminants pour l'évolution de la zone marginale sur des échelles saisonnières.

Équations du mouvement pour une zone marginale de glace idéalisée

Nous énumérerons ici quelques concepts et équations clés de la conceptualisation ayant mené au modèle pour la viscosité de cisaillement, mais le développement mathématique complet est présenté en détails au chapitre 1. Le modèle d'équilibre s'appuie sur le principe de conservation de la quantité de mouvement. Intégré sur la verticale pour la glace considérée comme un continuum bidimensionnel flottant sur l'océan, ce principe peut s'exprimer de la manière suivante

$$\rho_i h \left(\frac{D\mathbf{u}}{Dt} + f\hat{\mathbf{k}} \times \mathbf{u} \right) = \mathbf{F}_i - \nabla \cdot \boldsymbol{\sigma}. \tag{1}$$

où ρ_i est la masse volumique de la glace, h son épaisseur moyenne, $\mathbf{u} = u\hat{\mathbf{i}} + v\hat{\mathbf{j}}$ le champ de vitesse horizontal, $\mathbf{f} = f\hat{\mathbf{k}}$ est le paramètre de Coriolis et $\hat{\mathbf{k}}$ est la direction verticale, tel que $f\hat{\mathbf{k}} \times \mathbf{u}$ est l'accélération de Coriolis. L'opérateur D/Dt est la dérivée matérielle définie comme $\partial/\partial t + u\partial/\partial x + v\partial/\partial y$. Dans le terme de droite, $\mathbf{F}_i$ est la somme des forces externes s'exerçant sur la glace et $\nabla \cdot \boldsymbol{\sigma}$ représente la résistance interne de la glace. Cette dernière s'exprime comme la divergence du tenseur de contraintes de Cauchy qui prescrit la relation entre la déformation et les contraintes internes : ce terme caractérise la rhéologie du matériau.

En présence d'une marge stationnaire et en l'absence de formation ou de fonte de glace, le terme $D\mathbf{u}/Dt = 0$. On peut également négliger la pseudo-force de Coriolis devant les autres forces en jeu. En se basant sur les arguments de Sutherland and Dumont (2018) dont l'étude a été réalisée au même site et dans des conditions similaires, la force radiative domine sur les

autres forces. En effet, l'étude précédente constate que $\boldsymbol{\tau}_w$ domine sur la contrainte de vent sur une distance L_{WRS} qui s'exprime, en eaux profondes, telle que

$$L_{\text{WRS}} = \frac{\rho_w g}{32 \rho_a C_D} \left(\frac{H_s}{U_{10}} \right)^2 \tag{2}$$

où ρ_w et ρ_a sont respectivement les densités de l'eau de mer et de l'air, C_D est le coefficient de traînée aérodynamique de l'air, H_s est la hauteur significative des vagues et U_{10} est la vitesse du vent à une hauteur de 10m au-dessus de la surface. Pour les conditions observées et inclues dans l'analyse de cette thèse, la distance où la contrainte radiative des vagues domine sur le vent est estimée être de l'ordre de 4 km. Sutherland and Dumont (2018) ont aussi effectué une analyse dimensionnelle démontrant que la contrainte due aux vagues domine celle due aux courants. En assumant que la surface du fond marin est négligeable et que la glace n'est pas en contact avec celui-ci, la seule force externe affectant la zone marginale est $\boldsymbol{\tau}_w$.

De retour à notre raisonnement mathématique, on retrouve une équation décrivant l'équilibre entre les forces externes et la résistance de cette glace, i.e.

$$\boldsymbol{\tau}_w = \nabla \cdot \boldsymbol{\sigma} \tag{3}$$

Guardons en tête que dans la MIZ, la vitesse totale des *floes* de glace $\mathbf{u} = (u, v)$ peut aussi être décomposée comme $\mathbf{u} = \overline{\mathbf{u}} + \mathbf{u}'$ où $\overline{\mathbf{u}}$ est la vitesse moyenne temporelle, sur une période caractéristique plus longue que celle des vagues, et $\mathbf{u}'$ est la fluctuation de la vitesse associée principalement au mouvement orbital dû aux vagues de surface. Concernant le système de coordonnées, il est posé que l'axe des x est dans le sens normal à la lisière, c'est-à-dire perpendiculaire à la marge de glace et pointant vers l'intérieur de la MIZ. L'axe des y, quant à lui, est parallèle à la lisière et est aligné de telle sorte que $\hat{\mathbf{k}} = \hat{\mathbf{i}} \times \hat{\mathbf{j}}$ pointe vers le haut.

L'équation 3 constitue la base du modèle d'équilibre. En y injectant les formulations explicites de la contrainte radiative et des contraintes internes, ainsi qu'en utilisant le système de coordonnées énoncé ci-haut, on obtient l'équation suivante pour la viscosité de cisaille-

ment moyenne dans la zone marginale

$$\langle \eta \rangle = -\frac{1}{2}\rho_w g \cos\theta \sin\theta \left\langle \frac{\partial E}{\partial x} \right\rangle \left\langle \frac{\partial^2 \bar{v}}{\partial x^2} \right\rangle^{-1} . \tag{4}$$

Cette équation, dont la dérivation complète est présentée au chapitre 1, permet d'évaluer la viscosité d'une zone marginale de glace stationnaire avec vagues à incidence oblique et repose sur trois grandes hypothèses. La **première hypothèse** est que la marge de glace est stationnaire, ce qui implique que u est nul à $x = 0$, car la résistance en compression équilibre la contrainte normale provenant de la propagation des vagues. La **deuxième hypothèse** est que toute variation en y est nulle. On considère ici un fluide 2D intégré sur la verticale dont les composantes parallèles à la marge sont uniformes et ne dépendent que de la distance à la lisière x. Enfin, la **troisième hypothèse** est que η ne varie pas significativement sur l'échelle spatiale choisie et peut donc être considérée comme une constante. Nous verrons que cette dernière hypothèse n'est pas toujours appropriée, et la section 1.5 discute plus en détails de la validité de cette supposition, mais l'objectif est ici d'établir l'ordre de grandeur d'une quantité qui pour la glace peut en couvrir plusieurs selon les conditions.

Site d'étude

L'étude de la MIZ représente, de par sa définition, un véritable défi opérationnel. Cette zone, située à l'interface avec l'eau libre et décrite comme une banquise fragmentée, n'est pas facilement accessible, ni par bateau, ni de manière pédestre. Les expéditions à bord de brise-glaces sont possibles, mais représentent des expériences coûteuses, quoique bénéfiques à l'obtention de données en milieu éloigné. La capture de données graphiques peut s'effectuer avec l'usage de drones à partir de la rive, mais ceux-ci possèdent une portée maximale et une autonomie diminuant rapidement avec l'exposition de la batterie au froid (un froid nécessaire pour des conditions de glace optimales). Ceci rend donc difficile l'obtention de données sur les conditions à la lisière d'une durée de plus de dix minutes.

Afin de contrer la majorité de ces limitations, Dany Dumont (ISMER) a initié en 2014 un programme d'observations de la banquise nommé BicWin (Bic pour la proximité du Parc national du Bic et Win pour Winter) comprenant des campagnes de terrain annuelles. Pour effectuer des mesures in situ de glace et de vagues dans la MIZ, un canot à glace est utilisé depuis 2016 comme moyen de transport sécuritaire et efficace pour se faufiler dans tout type de paysage de la glace, qu'il soit statique ou mobile, lisse ou déformé. Ce véhicule permet de circuler à travers des glaces de toute concentration et de transporter de l'équipement tout en s'approchant de la lisière de glace de manière à augmenter la durée d'utilisation des drones au-dessus de la marge. Il permet aussi d'obtenir des mesures impossibles à obtenir en utilisant des plateformes de recherche traditionnelles, notamment de l'épaisseur de la glace à l'aide d'un conductivimètre (cette méthode ne sera pas décrite dans le cadre de ce mémoire).

Cette utilisation du canot à glace constitue une innovation dans l'accessibilité aux zones de glace non-consolidées, permet de familiariser les étudiants et scientifiques avec le terrain nordique et les conditions hivernales parfois difficiles, en plus de faciliter la recherche et l'obtention de données sur la MIZ. Plus spécifiquement, en se rapprochant de la marge de glace, la majorité des problématiques mentionnées précédemment entourant l'usage de drones sont éliminées et l'obtention de données visuelles (photos, vidéos) s'en voit grandement bonifiée.

FIGURE 1 – Canot à glace déployé dans la MIZ, vu d'un drone. On y voit 5 membres de l'équipage et des instruments de mesures, tel un ADCP (Acoustic Doppler Current Profiler) pour quantifier les fluctuations de vitesse, près de Saint-Fabien-sur-mer, Québec, Canada, le 12 février 2020. On peut aussi y observer la diversité de topographie, d'épaisseur et de taille des différents *floes* présents.

Dans le cas de la présente étude, le déploiement du canot s'est fait principalement à partir de la baie de Saint-Fabien-sur-mer, Québec, Canada. En 2018, le secteur de la Baie du Ha ! Ha ! (BdHH) a été utilisé comme laboratoire naturel par Sutherland and Dumont (2018) afin d'étudier l'impact de la contrainte des vagues arrivant dans un axe normal à la lisière de glace. La définition de cette zone d'étude permet de quantifier les propriétés matérielles de différents évènements de glace, tout en simplifiant plusieurs conditions.

FIGURE 2 – Image satellite de Saint-Fabien-sur-mer et ses environs, Québec, Canada, le 8 juillet 2023 à 15 : 39 : 49UTC. Source : Sentinel-2, Agence spatiale européenne (ESA).

La BdHH est une baie rectangulaire de 2 km de longueur par 1 km de largeur. L'Anse à Mercier est délimitée par l'Îlet au Flacon à l'est et s'étend sur environ 2.6 km vers l'ouest. Les profondeurs des deux secteurs se situent entre 5 m et 33 m. Les courants sont principalement attribuables aux épisodes de vents prolongés et aux marées, celles-ci pouvant varier de 0.6 m à 4.5 m au marnage maximal. Dû à l'orientation de la rive du fleuve à cet endroit, les vents de l'ouest peuvent avoir un fetch allant jusqu'à 80 km, menant ainsi à des vagues de plus forte amplitude et à des courants de surface plus élevés. De par son orientation, combinée aux vents dominants du sud-ouest durant l'hiver, ce secteur permet d'obtenir des conditions propices à la formation d'une MIZ possédant une lisière parallèle à la côte, avec des vagues générant du cisaillement.

Méthodologie générale

Dans le cadre de ce projet, la majorité des données a été obtenue à partir de drones déployés au-dessus de la marge de glace. Les données brutes sont sous forme de vidéos stationnaires s'étalant entre mars 2019 et février 2022. Des conditions de glace spécifiques étaient recherchées : une lisière serrée et des vagues entrant à incidence oblique. Un total de trente-deux (32) évènements ont été compilés, mais seulement onze (11) retenus, considérant la durée de la vidéo, l'illumination, la stabilité du vol, le type de glace et l'angle d'incidence des vagues. Le tableau 2 détaille les conditions de chaque vol et la section 1.4.1 décrit de manière spécifique leurs conditions de glace respectives. Les drones utilisés sont des DJI Mavic 2 Pro, avec une température d'opération entre $-10°C$ et $40°C$. Avec les conditions hivernales dans le fleuve Saint-Laurent, les températures ont souvent été sous la température minimale, diminuant ainsi la durée de vie de la batterie (durée de vol maximale moyenne de 25 minutes sans vent). L'entièreté des données provient des informations obtenues à partir des vidéos capturées. La méthodologie développée est schématisée à la Figure 3 et est décrite en détails dans le chapitre 1.

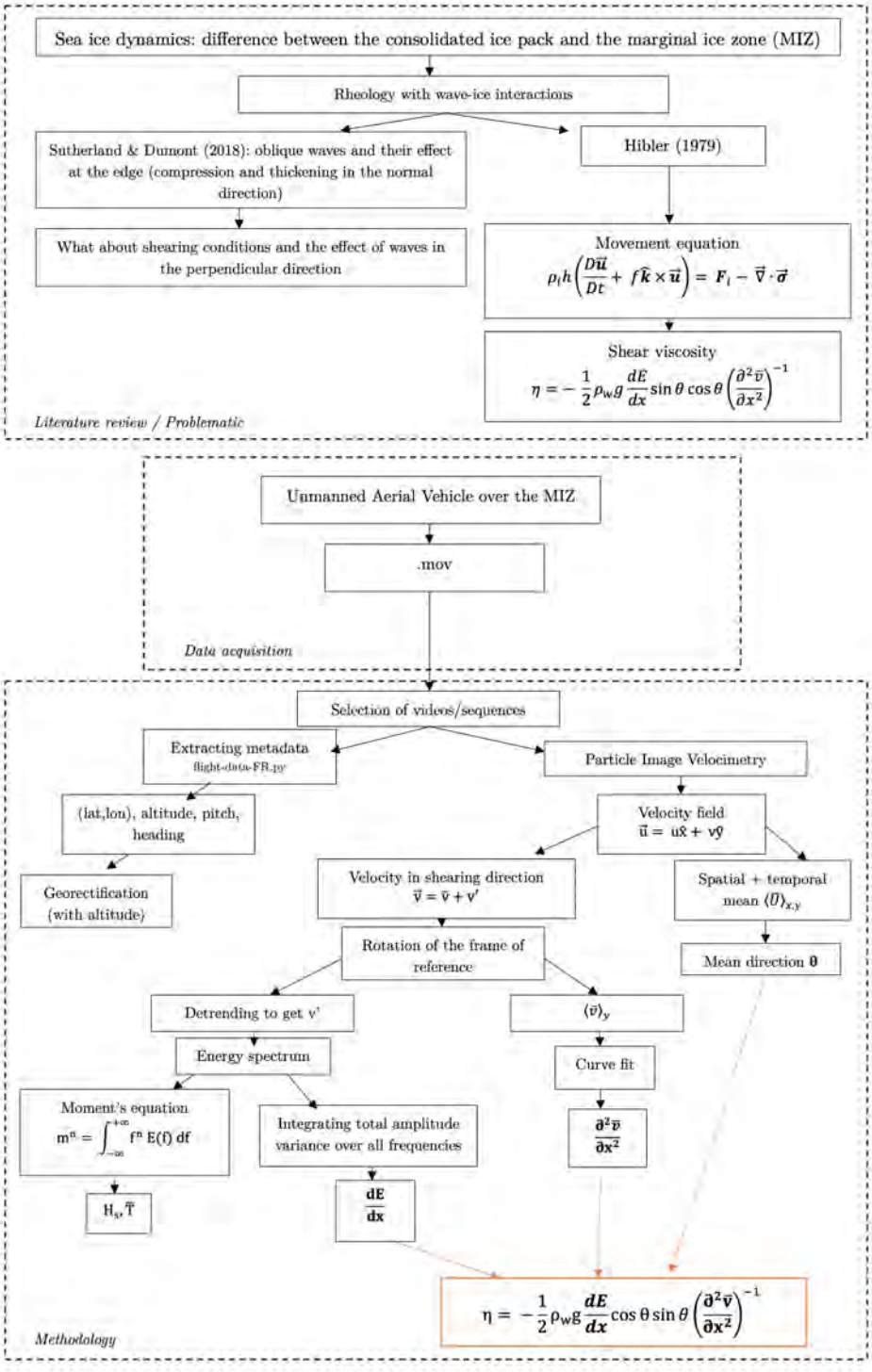

FIGURE 3 – Schéma méthodologique détaillant les différentes étapes de conceptualisation, acquisition des données et traitement subséquent jusqu'à l'application finale du modèle développé pour la viscosité de cisaillement.

ARTICLE 1

RHÉOLOGIE DE LA ZONE MARGINALE DE GLACE: MESURE DE LA VISCOSITÉ DE CISAILLEMENT DE LA GLACE DE MER EN PRÉSENCE DE VAGUES

Résumé en français du premier article

En déployant un aéronef télépiloté (ATP) près de la marge de glace dans l'estuaire du Saint-Laurent, des images aériennes de la propagation oblique de vagues dans la zone marginale de glace (MIZ) ont été obtenues. L'utilisation de la vélocimétrie par images de particules sur une sélection de onze (11) événements filmés a permis de quantifier plusieurs paramètres physiques, tels que la hauteur significative des vagues ($H_s \sim 1$ m), la période moyenne ($T \sim$ 3-4 s), l'angle d'incidence ($\theta \sim$ 22-48°) et le coefficient d'atténuation de l'énergie des vagues ($\tilde{\alpha} \sim O10^{-2}$) m^{-1}). Ces données sont utilisées pour contraindre un modèle d'équilibre entre les forces radiatives des vagues et les forces internes de la glace afin d'estimer, pour la première fois à partir d'observations directes, la viscosité de cisaillement ($\eta \sim O10^3$-10^4 kg s^{-1} de la zone marginale, en supposant celle-ci homogène. Toutefois seulement trois événements permettent d'obtenir une estimation quantitative, alors que les données des huit autres événements suggèrent que la viscosité de cisaillement n'est pas uniforme à travers la MIZ. L'application d'une technique de fenêtrage discret pourrait aider à développer et à améliorer le modèle proposé. La comparaison des valeurs obtenues avec deux modèles rhéologiques montre que la MIZ est mieux representée par une rhéologie granulaire de type Mohr-Coulomb que par la rhéologie visco-plastique qui est la plus largement utilisée dans les modèles de glace.

1.1 Introduction

2023 brings indisputable evidence of higher trending global temperatures, with a possibility over 99% of being the warmest year ever recorded according to the NOAA Global Climate Report of October 2023 (NOAA-NCEI, 2023). As temperature continues to rise, the Arctic is experiencing a warming rate roughly four times greater than the rest of the globe (Rantanen et al., 2022). Multiple studies have documented a decrease in both sea ice extent (SIE) (Stroeve et al., 2014; Cavalieri and Parkinson, 2012; Meier et al., 2005) and sea ice thickness (SIT) (Kwok and Rothrock, 2009). In addition to this reduction, recent years show an acceleration of the trend. Between 1998-2008, the decadal decline of perennal and seasonal Arctic SIE reached -10.1% to -10.7% in comparison to -2.2% to 3.0% per decade between 1979 and 1996 (Comiso et al., 2008).

The disappearance, even partial, of the summer ice cover in the Arctic is predicted to have cascading effects on the global climate, as the region plays a crucial role in general circulation. Alas, the recent work of Kim et al. (2023) showed the perspective of an ice-free summer (SIE below 1×10^6 km^2) near mid-century, highlighting the urgency to improve ice models in order to anticipate and characterize this considerable change.

Consequently, the Arctic sea ice has undergone a significant change with a transition from perennial ice to seasonal ice (Polyakov et al., 2012). In the 1980s, ice over 4 years old accounted for one-third of the Arctic pack composition. However, according to Perovich et al. (2021)'s work, this fraction has decreased drastically to approximately 4.4% in 2020. In his more recent work, Comiso et al. (2017) continued to characterize this drastic decrease and confirmed, by analyzing four satellite-derived sea ice data products, that the decline rate for perennial Arctic SIE reached 11% per decade. Kwok (2018) found that over the period of 1999-2017, the Arctic has lost more than 50% of its multi-year (over 2 years) ice. This study also presented a 60% thinning over six decades for the central Arctic summer mean SIT. While the summer mean is experiencing significant thinning, decrease in sea ice affects

the Arctic in all seasons, as demonstrated by Meier et al. (2014), Serreze et al. (2007) and numerous others. Additionally, recent research by Belter et al. (2020) reveals that modal ice thickness has decreased by more than 20% between 2001 and 2020.

This younger ice, surviving less and less summer melts, is increasingly brittle and prone to destruction by big storm events. With the declining ice becoming more fragile, more fetch is available for wave growth, resulting in the emergence of an increased Arctic wave climate (Thomson and Rogers, 2014). Over the past 20 years, the reduction in SIE led to higher wave heights and wavelengths, as well as more persistent swells (Stopa et al., 2016). These more energetic waves are hypothesized to contribute to increased fragmentation in the pack ice (Asplin et al., 2012), resulting in a smaller floe size distribution that could experience more rapid melting and drift (Squire, 2007). This also allows and favours deeper penetration of waves into the ice cover (Emmanuel et al., 2022).

Simply put, the marginal ice zone (MIZ) can be defined as the area of the sea ice cover affected by the open ocean (Wadhams et al., 1986). This region possesses multiple definitions and is supported by a wealth of literature that highlights the complexity of the processes driving its dynamics. Dumont (2022)'s review presents and details those different definitions, each evoking aspects or behaviors specific for the zone. Floes in the MIZ are usually described as modestly sized, densely packed, and often variable in composition. The MIZ can encompass both areas of ice production and ice consolidation, as well as contain leads and interstices. Processes such as rafting and ridging are not uncommon, and the highly dynamic conditions drive heat exchanges and interactions between the ocean, ice and atmosphere. Near the edge, it predominantly consists of younger ice, whether it be new ice, brash, nilas or ice in pancakes.

Waves exert a forcing on the ice cover by momentum transfer, a process known as the wave radiative stress (Longuet-Higgins and Stewart, 1964). They can travel hundreds of kilometers into the MIZ (Kohout et al., 2014), breaking up floes and exerting stress on the inner pack. This stress is proportional to the wave attenuation. As this attenuation is

strongest at the ice edge, i.e. at the junction between the open water and the ice pack, so is this stress (Dai et al., 2019). In the peripheral ice pack of the Southern ocean, the wave radiative stress may be dominant (Stopa et al., 2018) and hypotheses have been formed that it may become more and more significant in the Arctic as well (Boutin et al., 2020). Squire (2020) supported this hypothesis and suggested that, with the Arctic warming at an accelerated rate, the diminishing concentration of sea ice in the summer may start resembling the behaviour of sea ice in Antarctica.

Combining the growing wave-driven environment and the definition of the MIZ, one can predict that the spatial scale of this dynamic area will increase and hence, its understanding will become more and more important for the prediction of the future of sea ice in the Arctic. This assumption is reinforced by Aksenov et al. (2017) who stated that the intensification of the extent of the MIZ is to be expected, as well as by Boutin et al. (2020) suggesting that wave-ice interactions will need to be factored in as one of its dominant factor.

Wave propagation in ice-covered waters has been mainly studied theoretically and relies on multiple intertwined factors: dissipation, reflection, deformation, collisions, absorption, ice advection and so on, from which the difficulty for integration in models stems. Squire (1995, 2007, 2020) produced a series of reviews on wave-ice interactions showing the complexity of the coexisting processes to be incorporated. Cheng et al. (2020) also states that all these processes have yet to be fully integrated in models. The omission of these interactions is likely to lead to less accurate numeric simulations, as the parameterization of storms, winds and waves are contributing to the challenge (Stroeve et al., 2014). The discrepancy between model outputs and observations express the need for a better configuration for wave propagation through ice (Squire, 2018). On multiple occasions, research (Tietsche et al., 2014; Comiso et al., 2017) showed that sea ice models featured the most significant errors in the MIZ. While emerging studies regarding the MIZ dynamics have been unprecedented in the last decade, the relevance for a better understanding of wave-ice interactions has now been repeatedly shown.

One of the major limitation for quantifying and qualifying the MIZ is the scarcity of in situ observations (Ardhuin et al., 2015). The MIZ is difficult to access: the high ice concentration prevents most ships from navigating inly without disrupting the ice field and the lack of tautness between the pancakes and ice cakes makes travel afoot perilous. A few campaigns took place in the 80s and the 90s, with the Marginal Ice Zone EXperiment (MIZEX) being the first field exploration project in the MIZ of the Arctic Ocean (Johannessen, 1987; Rottier, 1989). It was followed by several others such as the Coordinated Eastern Arctic EXperiment (CEAREX) (Group, 1990), the Seasonal Ice Zone EXperiment (SIZEX) (Johannessen et al., 1990) in Fram Strait and the Labrador Ice Margin EXperiment (LIMEX) in the Labrador Sea (Liu et al., 1991).

The previously mentioned in situ datasets, while fundamental, were sampled in limited ice conditions. Even with the advent of remote sensing helping the quantitative characterization of sea ice in polar regions, Cooper et al. (2022) states that even current remote sensing datasets, while being studied and seeing recent progress by Stopa et al. (2018) and Brouwer et al. (2022), are not yet comprehensive and available. The use of unmanned aerial vehicle (UAV) also contributed to the advancement in the access of hazardous field environments, such as glacier crevasses (Chudley et al., 2019) and the MIZ (Dumas-Lefebvre and Dumont, 2023). While progress is constant and well underway, the need for field studies that simultaneously quantify wave propagation and attenuation in ice-covered waters is still present. Further research avenues for the MIZ are presented in the *Philosophical Transactions of the Royal Society* (RSTA) issue *Theory, modelling and observations of marginal ice zone dynamics: multidisciplinary perspectives and outlooks*, namely in Bennetts et al. (2022), Dumont (2022) and Squire (2022).

In this article, we focus on how sea ice, as a material, responds to the stress due to waves. Quantifying how the internal stress responds to a deformation rate is likely to impact how sea ice is modelled. Boutin et al. (2023) cites the work of Steele et al. (1997) to explain that the net transport of sea ice is driven by the parameterization of internal stress and

rheological terms in the momentum equation. Which rheology is to be applied is an important aspect to consider if one wants to obtain accurate prediction of sea ice behaviour. The most widely used rheology in global climate and large-scale ice-ocean models is the viscous-plastic (VP) formulation derived from the seminal work of Hibler (1979). It is followed by the elastic-viscous-plastic (EVP) formulation documented by Hunke and Dukowicz (1997) and modified by Lemieux et al. (2012). Hibler (1979)'s elliptical yield curve is based on the hypothesis that sea ice under compressive or shearing conditions will react as a plastic material, hence where stresses will be proportional to deformations. It implies that internal constraints are entirely resolved at the model scale, leading to localized shearing zones. While this rheology is still widely used and reproduce reasonably well mean ice drift and thickness, as shown by Zhang and Hunke (2001), numerical ice models still present error for small-scale deformations. Kwok et al. (2008) support this statement and argue for the necessity for high-resolution ice drift observations. Other formulations have been proposed and studies, such as the elasto-brittle (EB) for predicting fractures (Bouillon and Rampal, 2015) the granular rheology (Feltham, 2005; Jop et al., 2006) recently reviewed by Herman (2022), including the Mohr-Coulomb formulation (Uzuner and Kennedy, 1976; Dai et al., 2004).

Each rheology formulation has a number of physical parameters and viscosity is one of those. It determines how a material enduring a stress deforms and transmits momentum in various directions. Ice viscosity can be associated to different underlying dissipative mechanisms: eddy viscosity refers to eddy formation and subsequent dissipation beneath an ice floe, bulk viscosity refers to normal (compressive) deformations, and shear viscosity is associated to shearing conditions, which can involve sliding but also floe-floe interactions (collisions) or other internal stresses (bending) and deformation (Doble et al., 2015). Ideally, viscosity parameters should account for all types of dynamical regimes, which would most certainly require that they depend on sea ice material and mechanical properties such as floe size and thickness. Doing so could lead to a better representation of ice dynamics closer to the edge and hence, to better predictions regarding the edge position, ice transport and so on.

Recently, Sutherland and Dumont (2018) laid the basis for our present work by studying the dynamic equilibrium between the wave radiation and the compressive strength using in situ data from a marginal ice zone in the St. Lawrence Estuary. They found that the Mohr–Coulomb granular rheology and more specifically the quadratic dependence of the compressive strength on ice thickness (Uzuner and Kennedy, 1976) was well-suited for the marginal ice zone and fitted quite well the measured thickness profile. Their model was validated and tested for normal wave incidence, but did not cover oblique wave incidence leading to shearing conditions. The work of Thomson et al. (2021) address a similar situation as ours. They devised a model for a sheared MIZ based on similarities shared with the surf zone and used a predetermined ice shear viscosity value of 10^2 m^2 s^{-1} to derive an ice-ocean viscous drag model in the presence of waves.

Here, we propose to estimate the shear viscosity of the marginal ice zone using a purely empirical approach for a Reiner-Rivlin formulation of a generalized Newtonian fluid (Hakkinen, 1987). In other words, no rheological model is specified a priori. The method we propose uses an UAV to simultaneously quantify the deformation near the ice edge and the radiative stress coming from the obliquely-incident wave train. The experimental site is located near Saint-Fabien-sur-mer, QC, Canada, which is particularly prone to MIZ conditions.

We organized this article into a logical framework: section 1.2 discusses the conceptual framework used for an idealized MIZ, the methods are reported in section 1.3, the results are shown by presenting one event as an example in section 1.4, where we also included the main physical properties measured for each event. Section 1.5 presents further discussions and future work perspectives, and lastly, in section 1.6 we conclude and summarize the main findings.

1.2 Conceptual framework

In this section we develop a mathematical model describing the dynamic equilibrium of a stationary marginal ice zone where external forces applied to the ice are balanced with its internal rheological response. The aerial picture displayed in Figure 4 is an example of such a situation. We thus suppose that oceanic and atmospheric conditions are stationary or vary slowly in time and are such that the ice does not grow or melt significantly over time. We also assume that environmental conditions vary slowly in space compared to the extent of the marginal ice zone. Since waves are the main driver of the MIZ dynamics considered in this work, a suitable time scale is the time required for waves to travel across the MIZ, and the spatial scale is set by the attenuation decay length of the longest waves hitting the MIZ.

The following mathematical development stems from three main assumptions. First, the ice edge is stationary, which means that ice thickness, concentration and floe size variations across the MIZ are such that the ice resists to the normal compressive forces applied by waves. Mathematically, it means that $u(x, y, t) = 0$. Second, the MIZ is uniform in the direction along the ice edge such that variations along the y-axis are null. The third assumption is that the effective shear viscosity is considered to be varying slowly over the sampling area. This allows us to consider that $\frac{\partial \eta}{\partial x} \rightarrow 0$ to a first approximation that could be relaxed depending on results. Since this is a first attempt to estimate the effective shear viscosity, considering it is slowly varying or even uniform still allows for obtaining quantitative results. The equilibrium model is derived in the next sections, starting with laying out the general momentum equation for sea ice and progressively applying it to an idealized MIZ.

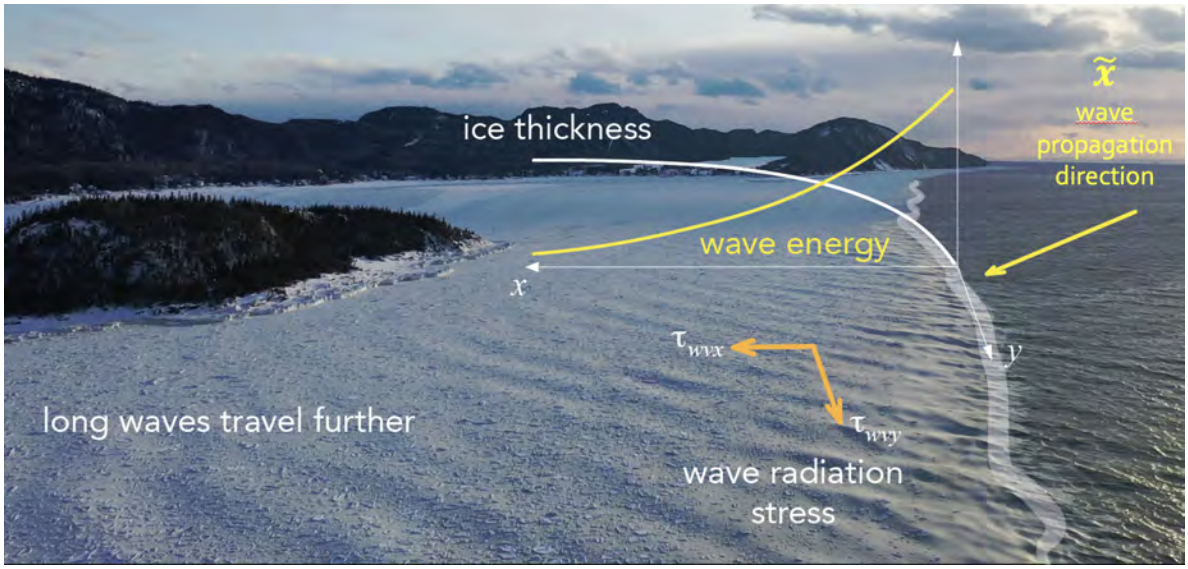

Figure 4 – Aerial picture of the marginal ice zone off Anse-à-Mercier, Saint-Fabien-sur-mer, Québec, Canada on March 7, 2019, 16:37 EDT. Air temperature is $T_{\text{air}} \simeq -11°\text{C}$ and the wind is blowing from the west (~270°) at 30 km h^{-1}, according to the Environment Canada weather station of Pointe-au-Père. The ice edge is highlighted by the white band. Waves are progressively attenuated as they propagate in the MIZ, with short waves being attenuated more rapidly than longer waves.

1.2.1 Equilibrium momentum equations for an idealized MIZ

The vertically-integrated momentum balance equation for sea ice floating at the ocean surface is expressed as (Lemieux et al., 2017)

$$\rho_i h \left(\frac{D\mathbf{u}}{Dt} + f\hat{\mathbf{k}} \times \mathbf{u} \right) = \mathbf{F}_i - \nabla \cdot \boldsymbol{\sigma} \tag{1.1}$$

where ρ_i is ice density, h is the mean thickness, $\rho_i h$ corresponds to the ice mass per unit surface, $\mathbf{u} = u\hat{\mathbf{i}} + v\hat{\mathbf{j}}$ is the horizontal velocity field of the ice, and $f\hat{\mathbf{k}} \times \mathbf{u}$ the Coriolis acceleration. In the context of the MIZ where waves put the ice in an oscillatory motion, it is convenient to partition the velocity field $\mathbf{u}$ into a mean velocity field $\overline{\mathbf{u}}$, averaged over a time scale that is much longer than the characteristic wave period, and a fluctuation velocity field

$\mathbf{u}'$ that include the motion associated to the wave orbital movements and other fluctuations arising from floe-floe interactions. The second term of the right-hand side $\nabla \cdot \boldsymbol{\sigma}$ corresponds to the divergence of the Cauchy stress tensor $\boldsymbol{\sigma}$ describing the stresses acting on the ice on the horizontal plane. It is a second-order tensor with four components σ_{ij}, with the divergence defined as

$$\nabla \cdot \boldsymbol{\sigma} = \frac{\partial \sigma_{ij}}{\partial x_i} \hat{\mathbf{e}}_j = \left(\frac{\partial \sigma_{11}}{\partial x} + \frac{\partial \sigma_{21}}{\partial y} \right) \hat{\mathbf{i}} + \left(\frac{\partial \sigma_{12}}{\partial x} + \frac{\partial \sigma_{22}}{\partial y} \right) \hat{\mathbf{j}}. \tag{1.2}$$

Finally, the first term on the right-hand side $\mathbf{F}_i$ refers to the sum of all external forces applied to the ice per unit area. There are five forces that are typically distinguished

$$\mathbf{F}_i = \boldsymbol{\tau}_g + \boldsymbol{\tau}_a + \boldsymbol{\tau}_o + \boldsymbol{\tau}_b + \boldsymbol{\tau}_w \tag{1.3}$$

$\boldsymbol{\tau}_g$ is the net force applied by gravity along a tilted ocean's surface, $\boldsymbol{\tau}_a$ is the stress due to the wind, $\boldsymbol{\tau}_o$ is the stress due to ocean currents, $\boldsymbol{\tau}_b$ comes from the friction with the sea bed and $\boldsymbol{\tau}_w$ is the wave radiative stress. Its incorporation in sea ice models is fairly recent as it requires information from a wave model. The effect of this force, and more generally the multiple effects waves have on sea ice, have only been researched in the field by a few studies. As mentioned previously, our work is largely inspired by Sutherland and Dumont (2018) who derived an equilibrium model for ice thickness in marginal ice zones similar to the one we examine here. They found that the wave radiative stress (WRS) dominates the direct wind stress over a distance L_{WRS} that scales, in deep water, as

$$L_{\mathrm{WRS}} = \frac{\rho_w g}{32 \rho_a C_D} \left(\frac{H_s}{U_{10}} \right)^2 \tag{1.4}$$

where ρ_w and ρ_a are respectively sea water and air densities, C_D is the air drag coefficient, H_s is the significant height of incident waves and U_{10} is the 10-m wind speed. For the conditions that prevail during the events analyzed, L_{WRS} and l_α, i.e. the e-folding scale of wave damping given by $1/\alpha$, were respectively estimated to be the order of 4 km and 140 m. Sutherland

and Dumont (2018) also carried out a similar dimensional analysis to show that the WRS significantly overcomes the stress due to ocean currents. As we will see later, this assumption is less stringent as we only require that the current shear is weak, not the current itself, like is also done by Thomson et al. (2021). Assuming that the surface slope is negligible and that the ice never touches the seabed, the only external force that affects the marginal ice zone is $\boldsymbol{\tau}_w$. Recalling the assumption that the MIZ is in a stationary equilibrium and that the Coriolis force is negligibly small compared to $\boldsymbol{\tau}_w$, equation 1.1 reduces to

$$\boldsymbol{\tau}_w - \nabla \cdot \boldsymbol{\sigma} = 0. \tag{1.5}$$

Using equation 1.2, 1.5 can be written in Cartesian coordinates as

$$\begin{aligned} \tau_{wx} &= \frac{\partial \sigma_{11}}{\partial x} + \frac{\partial \sigma_{21}}{\partial y} \\ \tau_{wy} &= \frac{\partial \sigma_{22}}{\partial y} + \frac{\partial \sigma_{12}}{\partial x}. \end{aligned} \tag{1.6}$$

The next step consists in determining a formulation for the stress tensor components, which requires a constitutive law for sea ice. The most common and general framework that is used to build such constitutive law, also referred to as the rheology, is the Reiner-Rivlin theory. This theory, developed and formulated by Reiner (1945) and Rivlin (1948), is based on the generalized theory for Newtonian fluids where viscosity parameters are functions of the strain rate and other material variables. The most general and complete formulation for a two-dimensional Reiner-Rivlin compressible fluid, as demonstrated by Hakkinen (1987) and used in most sea ice dynamics models since the seminal work of Hibler (1979), is given by

$$\sigma_{ij} = 2\eta\dot{\varepsilon}_{ij} + (\zeta - \eta)\dot{\varepsilon}_{kk}\delta_{ij} - \frac{P}{2}\delta_{ij}. \tag{1.7}$$

where η and ζ are shear and bulk viscosity coefficients, P is an isotropic pressure term, δ_{ij} is the Kronecker delta function and $\dot{\varepsilon}_{ij}$ is the strain rate tensor defined as

$$\dot{\varepsilon}_{ij} = \frac{1}{2}\left(\frac{\partial u_i}{\partial x_j} + \frac{\partial u_j}{\partial x_i}\right). \tag{1.8}$$

Using 1.7 and 1.8, we can rewrite 1.6 in its most general form as

$$\begin{aligned}
\tau_{wx} &= \frac{\partial}{\partial x}\left[\eta\left(\frac{\partial u}{\partial x} - \frac{\partial v}{\partial y}\right) + \zeta\left(\frac{\partial u}{\partial x} + \frac{\partial v}{\partial y}\right) - \frac{P}{2}\right] + \frac{\partial}{\partial y}\left[\eta\left(\frac{\partial u}{\partial y} + \frac{\partial v}{\partial x}\right)\right] \\
\tau_{wy} &= \frac{\partial}{\partial y}\left[\eta\left(\frac{\partial v}{\partial y} - \frac{\partial u}{\partial x}\right) + \zeta\left(\frac{\partial u}{\partial x} + \frac{\partial v}{\partial y}\right) - \frac{P}{2}\right] + \frac{\partial}{\partial x}\left[\eta\left(\frac{\partial u}{\partial y} + \frac{\partial v}{\partial x}\right)\right].
\end{aligned} \tag{1.9}$$

The behaviour of the generalized Newtonian material is determined by the specific form parameters P, η and ζ take. In the ice rheology of Hibler (1979), the compressive strength P is proportional to the mean ice thickness h and decays exponentially with ice concentration A, such that $P = P^\star h e^{-C^\star(1-A)}$ where $P^\star$ and $C^\star$ are constants. Using the argument that at a certain scale stochastic plastic deformations can be averaged to viscous behaviour, Hibler (1977) proposes that η and ζ are functions of the strain rate and proportional to P. For an elliptical yield curve, which corresponds to the stress state where the material undergoes plastic deformation, $\zeta = e^2\eta = P/2\Delta$, where Δ is a function of strain rate components. Hibler's model has been developed and applied mostly to represent and simulate sea ice dynamics at a large scale.

In the marginal ice zone, when the ice cover is a jumble of ice floes interspersed with brash, the compressive strength instead seems to follow a quadratic dependence on the mean thickness. According to Uzuner and Kennedy (1976), Dai et al. (2004) and more recently by Sutherland and Dumont (2018), for a compact ice jumble,

$$P = \frac{\rho_i g h^2}{2}\left(1 - \frac{\rho_i}{\rho_w}\right)(1-n)\left(\frac{1+\sin\phi}{1-\sin\phi}\right) \tag{1.10}$$

where ϕ is the internal friction angle and n is the jumble porosity. For the MIZ, however, the

effective viscosities were not quantified. In the following, we leave them undetermined as the objective is to estimate their value.

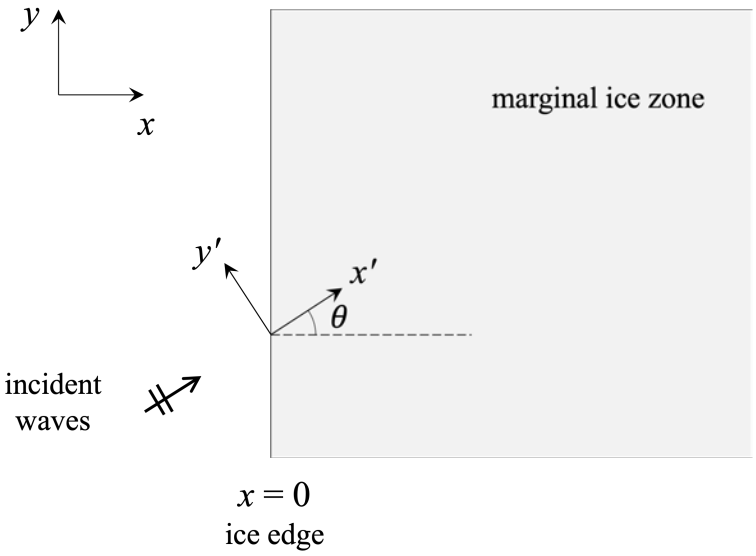

Figure 5 – Schematic top view representation of a stationary marginal ice zone hit by surface gravity waves. The main coordinate system is described by (x, y), with the axis respectively perpendicular and parallel to the edge. (x', y') refer to a rotation of this system in order to be aligned with the direction of wave propagation. θ is the angle of incidence of the waves and $x = 0$ delimits the ice edge.

Before introducing the specific form of the wave radiative stress, we can readily simplify equation 1.9 to the particular situation illustrated in Figure 5. We recall our assumptions that the ice edge is stationary and all dynamical and material quantities are homogeneous in the direction along the ice edge, which means that $u = 0$ and that all y-derivatives are null, leading to

$$\begin{aligned} \tau_{wx} &= \frac{1}{2}\frac{\partial P}{\partial x} \\ \tau_{wy} &= \frac{\partial}{\partial x}\left(\eta \frac{\partial v}{\partial x}\right). \end{aligned} \tag{1.11}$$

Now we can expand the wave radiation stress, which is also expressed as the divergence of a

second-order tensor defined as (Longuet-Higgins and Stewart, 1964)

$$\boldsymbol{\tau}_w = -\nabla \cdot \mathbf{R} = -\frac{\partial R_{ij}}{\partial x_i}\hat{\mathbf{e}}_j. \tag{1.12}$$

For waves incident at an angle θ and having an energy $\rho_w g E$, with E having units of amplitude squared,

$$\mathbf{R} = \begin{bmatrix} R_{11} & R_{12} \\ R_{21} & R_{22} \end{bmatrix} = \rho_w g E \begin{bmatrix} \frac{c_g}{c}\cos^2\theta + \left(\frac{c_g}{c} - \frac{1}{2}\right) & \frac{c_g}{c}\cos\theta\sin\theta \\ \frac{c_g}{c}\cos\theta\sin\theta & \frac{c_g}{c}\sin^2\theta + \left(\frac{c_g}{c} - \frac{1}{2}\right) \end{bmatrix} \tag{1.13}$$

where c_g and c are respectively the group and phase speed of the waves. Using the fact that in deep water $c_g = c/2$ and computing the Cartesian components of the wave radiative force, equation 1.11 becomes

$$\begin{aligned} \rho_w g \frac{\partial E}{\partial x}\left(\frac{1}{2}\cos^2\theta\right) + \frac{1}{2}\frac{\partial P}{\partial x} &= 0 \\ \rho_w g \frac{\partial E}{\partial x}\left(\frac{1}{2}\cos\theta\sin\theta\right) + \frac{\partial}{\partial x}\left(\eta\frac{\partial v}{\partial x}\right) &= 0. \end{aligned} \tag{1.14}$$

Regarding the deep water approximation necessary to obtain the above-mentioned form, we executed a quick analysis of the wave train in our field of study for each event. According to the marine charts, the smallest water depth below chart datum for all 11 events is around 7 m, and 7.5 m when considering the tide level (see Figure 6). At this depth, the dominant waves having 20-35 meter wavelength (where most of the energy is) are within 5% of the deep water dispersion.

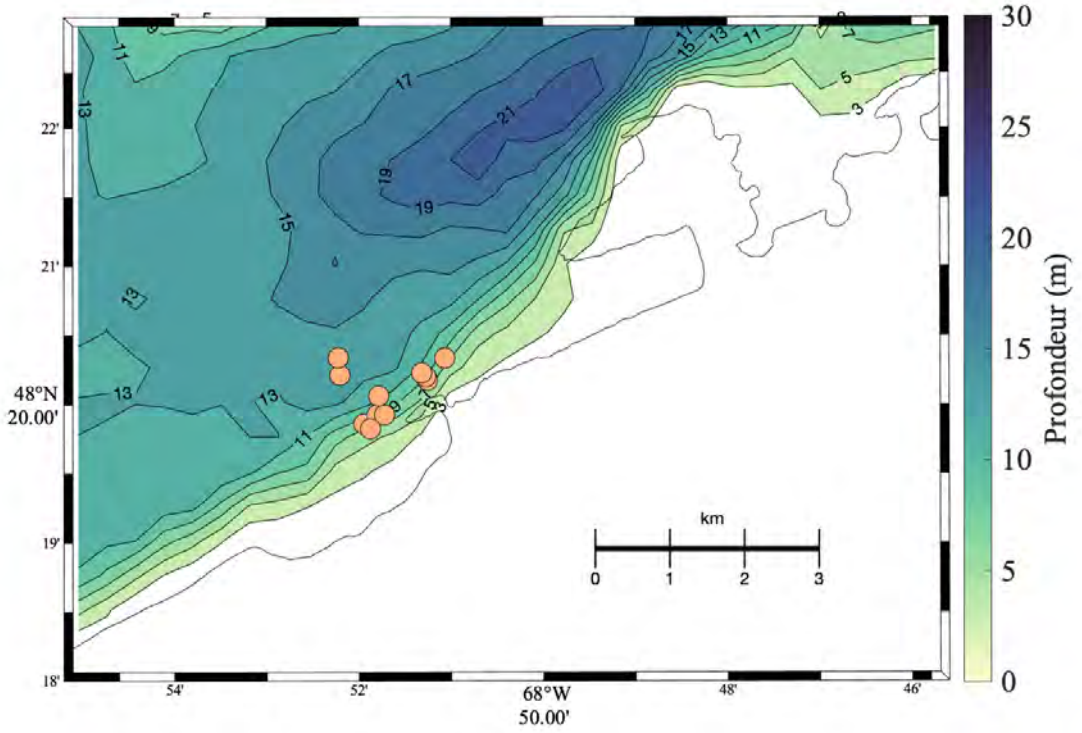

Figure 6 – Location of all 11 events overlaid on bathymetric data.

Going back to the set of equations 1.14, it describes two equilibria: 1) a static equilibrium between the radiative force normal to the ice edge and the compressive strength of the marginal ice zone, which was studied quantitatively by Sutherland and Dumont (2018), and 2) a shear equilibrium between the wave radiative force and internal ice friction, or, when the strain rate does not vanish, shear viscous forces. In principle, $\partial E/\partial x$ and η vary along the x-axis. In this case, estimating η would involve solving a first-order differential equation. As a first attempt to estimate the magnitude of the effective viscosity, we instead assume that it is constant over the region of interest, i.e. $\partial\eta/\partial x \simeq 0$, which allows us to invert equation 1.14 and obtain the following expression for the mean shear viscosity

$$\langle \eta \rangle_x = -\frac{1}{2}\rho_w g \cos\theta \sin\theta \left\langle \frac{\partial E}{\partial x} \right\rangle_x \left\langle \frac{\partial^2 \overline{v}}{\partial x^2} \right\rangle_x^{-1} . \tag{1.15}$$

1.2.2 Parameters and variables

The following Table 1 regroups the different parameters and variables used in the previous mathematical development. Spatial averages are denoted by angular brackets such as $\langle v \rangle_{x_i}$, while time averaging is represented by an overline variable $\overline{v}$.

Table 1 – Variables and parameters used in this document.

Variable	**Symbol**	**Units**
Velocity field	$\mathbf{u}$	m s^{-1}
Orbital velocity	$\mathbf{u}'$	m s^{-1}
Mean velocity	$\langle \overline{U} \rangle_{x,y}$	m s^{-1}
Mean along-edge velocity	$\langle \overline{v} \rangle_{y}$	m s^{-1}
Wave incidence angle	θ	deg
Wavenumber	k	m^{-1}
Internal friction angle	ϕ	deg
Mean ice thickness	h	m
Ice concentration	A	-
Ice strength	P	Pa m
Ice internal stress tensor	σ_{ij}	Pa m
External stress vectors	$\boldsymbol{\tau}_i$	Pa
Strain rate tensor	$\dot{\varepsilon}_{ij}$	s^{-1}
Wave radiative tensor	$\mathbf{R}$	Pa
Apparent wave energy attenuation coefficient	$\tilde{\alpha}$	m^{-1}
Wave energy attenuation coefficient	α	m^{-1}
Mean amplitude variance	$\langle \overline{a^2} \rangle_{y}$	m^2
Ice jumble porosity	n	-
Air drag coefficient	C_D	-
Frequency of the ith Fourier mode	f_i	Hz
Phase of the ith Fourier mode	ϕ_i	deg
Bulk ice viscosity	ζ	kg s^{-1}
Shear ice viscosity	η	kg s^{-1}
Parameter	**Symbol**	**Value**
Water density	ρ_w	1025 kg m^{-3}
Air density	ρ_a	1.293 kg m^{-3}
Gravitational acceleration	g	9.81 m s^{-2}

1.3 Methods

Solving equation 1.15 and estimating the shear viscosity requires measuring three quantities: the angle of incidence θ, the wave energy attenuation perpendicular to the ice edge $\frac{\partial E}{\partial x}$ and the second-order derivative of the mean along-edge velocity $\frac{\partial^2 \bar{v}}{\partial x^2}$. We used aerial drone imagery to estimate these values by recording stationary videos near the ice edge from a fixed altitude with a 90° pitch. We used DJI Mavic 2 Pro unmanned aerial vehicle (UAV), proven reliable in cold temperatures for similar experiments [e.g. Dumas-Lefebvre and Dumont (2023)], to record 4K videos with the integrated Hasselblad camera. Videos and flights metadata (altitude, GPS coordinates, camera orientation) are used to obtain georectified information at a fairly high resolution (a few centimeters). The drone used automatically corrects video distortion (DJI, 2018) and a calibration was done a priori.

The ice velocity field $\mathbf{u}(x, y, t)$ is extracted using particle image velocimetry (PIV), a method also called digital image correlation (DIC). For this, we used the open-source PIVLab Matlab toolbox (Thielicke and Stamhuis, 2014). The total velocity field $\mathbf{u}(x, y, t)$ is then decomposed as the sum of a time-averaged component $\overline{\mathbf{u}}(x, y)$ and a fluctuation component $\mathbf{u}'(x, y, t)$. In the context of a stationary ice edge, the direction of the mean velocity field should be nearly the same everywhere, and pointing in the along-ice-edge direction. It allows selecting the coordinate system (x, y) such that $\langle \overline{\mathbf{u}} \rangle = (0, \langle \bar{v} \rangle)$. It is thus desirable that the drone is indeed oriented as much as possible orthogonal to this system, with the widest image dimension oriented across the MIZ.

The fluctuation velocity captures the wave-induced orbital motion of sea ice, which we can use to estimate the wave energy spectrum $\rho_w g E(x, y)$, where E is the variance of surface elevation. The mechanical wave energy per unit of ocean surface for a sinusoidal wave of amplitude a is $\rho_w g a^2/2$. For irregular waves with random amplitudes and phases, the mechanical wave energy is $\rho_w g \overline{a_i^2/2}$ where a_i are the components of the Fourier series of the

surface elevation time series

$$\xi(t) = \sum_{i=1}^{N} a_i \cos\left(2\pi f_i t + \phi_i\right) \tag{1.16}$$

f_i and ϕ_i are respectively the frequencies and phases of the i^{th} Fourier mode. Assuming that wave propagation in the marginal ice zone is the same as in deep open water, which is nearly the case as shown by Sutherland and Dumont (2018) in similar conditions, the surface orbital velocity $\mathbf{u}$ is related to the wave amplitude a through $\mathbf{u} = a\mathbf{k}/k\omega$, where $\mathbf{k}$ is the vector wavenumber of magnitude $k = 2\pi/\lambda$, and $\omega = 2\pi f$. If $E_u(x, y, f)$ is the spectrum of the x-component of the surface velocity obtained from the PIV analysis, then $E(x, y, f) = E_u(x, y, f)/\omega^2$. The total wave elevation variance spectrum $E(x, y)$ is finally obtained by integrating over the frequency domain. However, to avoid taking into account ice motion that would not be caused directly by wave orbital motion but rather caused by floe-floe interactions, which cause noise in both the low and high frequency domains, the integration is done between 0.2 and 0.5 Hz.

Figure 7 shows the expected distribution of the wave energy in the MIZ for different incidence angles, but for similar wave dissipation rate $\alpha = 2.6 \times 10^{-2}$ m^{-1} and incident energy $E_0 = 0.1$ m^2. One can note that the wave energy field doesn't vary along the y-axis, but decline exponentially along the x-axis at an apparent decay rate $\tilde{\alpha} = \alpha \sec\theta$. In such an idealized case, i.e. when the incident wave spectrum is stationary and homogeneous, and when the wave dissipation rate is constant, the wave energy field follows

$$\begin{aligned} E(x) &= E_0 e^{-\tilde{\alpha}x} \\ \frac{\partial E}{\partial x} &= -\tilde{\alpha} E(x). \end{aligned} \tag{1.17}$$

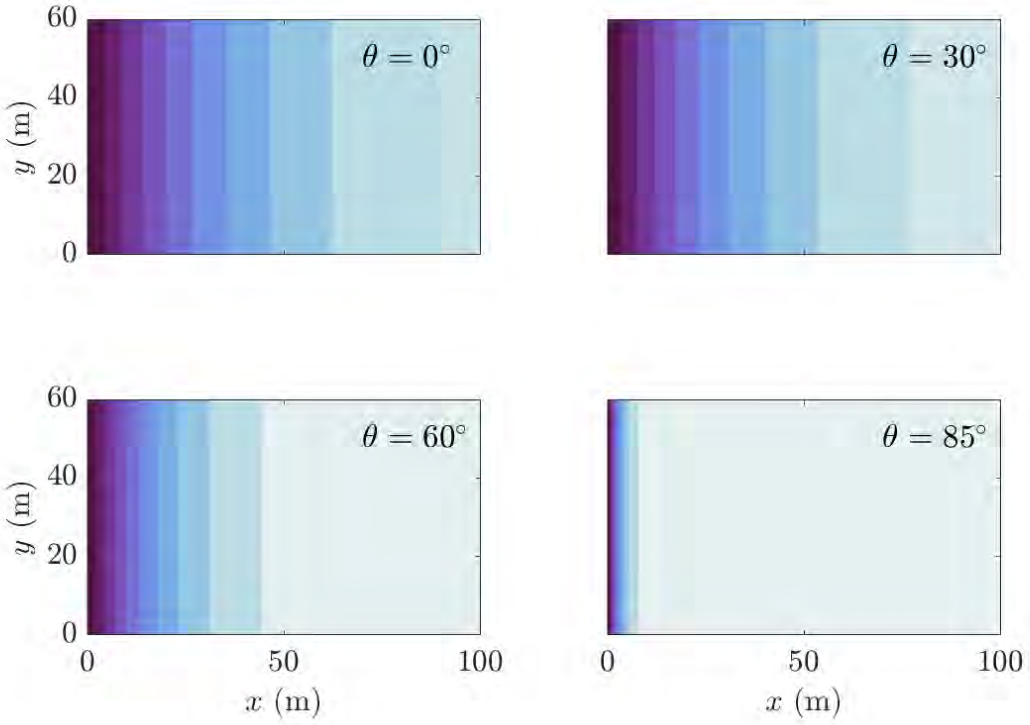

Figure 7 – Total wave energy distribution in the MIZ for $E_0 = 0.1$ m^2 and $\alpha = 2.6 \times 10^{-2}$ m^{-1}, pertaining to different incidence angle θ.

1.3.1 Study site and environmental conditions

Field experiments were conducted in Quebec's Bic National Park, located on the southern shore of the St. Lawrence Estuary, as part of the annual BicWin campaigns (Sutherland and Dumont, 2018) from 2019 to 2022. The experiments were carried out from the end of February to the beginning of March. Flights were performed near Baie du Ha! Ha!, a 1 km by 2 km embayment located in the western part of the park. It faces west toward an area with less ice coverage than in other regions of the Estuary due to the existence of a sensible heat polynya driven by tides at the head of the Laurentian channel, located 60 km westward. This area is thus prone to wind wave generation even during winter, where the fetch can reach up

to 80 km. This phenomenon is documented by the Canadian Ice Service (CIS) archives over the years 1990-2020 that indicates the presence of an area with lesser ice concentration (10-60%) at the head of the Laurentian Channel for the weeks between February 19 and March 12, while the remainder of the Estuary is reported as a very close drift (90-100% as per the World Meteorological Organization definition (WMO, 2014)). This sensible heat polynya, also documented by Saucier et al. (2003), is one of the key component in making this site particularly interesting for the study of wave-ice interactions.

A total of thirty-two events with aerial drone video footages of the MIZ were compiled, but only eleven events were selected considering criteria such as illumination, video length, flight stability, ice type and wave incidence angle. Parameters of the flights are described in Table 2 and ice conditions are shown in snapshots in Figure 8.

By extracting the frames of each event and processing them with the PIVLab GUI based open-source MatLab toolbox (Thielicke and Stamhuis, 2014), we apply a planar Digital Particle Image Velocimetry (2D PIV). PIV is a non-intrusive technique that allows characterizing the displacement of objects and patterns in a sequence of images. This technique has been extensively used in recent years for flow analysis (Sarno et al., 2018; Yamamoto and Ishikawa, 2022; Thielicke and Sonntag, 2021).

1.4 Results

1.4.1 Ice conditions

Before describing the ice conditions of the selected events themselves, let's first depict the general ice characteristics present in a typical MIZ. As stated previously, ice composition near the edge typically includes younger ice types, such as new ice, brash, nilas, or ice in pancakes. Pancake ice, defined by the WMO (2014) as greater than 30 cm but less than 3 m wide, typically provides a valid viscosity approximation in a generalized MIZ context.

Table 2 – UAV flight and photogrammetric data.

Event	Date and Time	Latitude	Longitude	Altitude	Heading	Pitch	Resolution	Length	Width	Duration
	UTC	°N	°W	m	° relative to N	°	cm px^{-1}	m	m	s
1	2019-03-05T16:02:13	48.336262	68.854307	92.6±0.3	223.6±0.4	-90.0±0.1	3.10±0.01	119.17	67.03	96
2	2019-03-05T16:04:13	48.336616	68.854542	92.7±0.5	227.4±0.6	-89.9±0.1	3.11±0.02	119.24	67.07	65
3	2019-03-05T16:06:03	48.337195	68.855330	92.7±0.5	227.4±0.4	-90.0±0.1	3.11±0.02	119.25	67.08	128
4	2019-03-07T16:31:18	48.338940	68.851104	96.6±1.2	245.0±2.5	-89.9±0.1	3.24±0.04	124.32	69.93	301
5	2022-02-20T18:03:34	48.331030	68.865750	189.7± 2.0	234.3±1.5	-90.0±0.1	6.35±0.07	244.00	137.25	422
6	2022-02-20T20:58:33	48.336884	68.870145	194.5±0.6	240.4±0.8	-89.9±0.1	6.52±0.02	250.21	140.74	373
7	2022-02-20T21:52:56	48.339018	68.870392	209.4±0.5	220.7±0.7	-89.6±0.1	7.01±0.02	269.33	151.50	482
8	2022-02-21T16:07:07	48.332121	68.863430	187.5±0.9	219.2±2.9	-90.0±0.1	6.28 ±0.03	241.18	135.66	301
9	2022-02-21T16:22:07	48.332088	68.862070	188.7±0.8	219.5±2.6	-90.0±0.1	6.32±0.03	242.71	136.53	361
10	2022-02-21T17:02:58	48.330358	68.864596	190.5±0.7	227.1±1.4	-90.0±0.1	6.38±0.02	245.02	137.82	388
11	2022-02-24T18:52:11	48.334350	68.863160	199.3±3.5	234.4±0.9	-88.0±0.1	6.7±0.1	256.38	144.21	301

New ice, such as frazil ice that is present in greater quantities in the MIZ than in the inner pack (Dumont et al., 2011), does not have a shape, but can be modelled as a polydisperse fluid. Brash, an accumulation of broken-up ice floes of various stages of development, is a common term used in the MIZ literature to qualify the ice and, per the WMO (2014)'s definition, is below 2 m in size which also meets the criteria for a viscous representation mentioned above. The presence of brash at the ice edge has been previously observed, with documented instances such as Webber (1987) referring to the MIZ consistency as a *highly concentrated brash-like viscous soup of small ice cakes*.

Along the southern shore of the St. Lawrence Estuary, the 30-year climatology compiled by the Canadian Ice Service indicates a trace of medium first-year ice (up to 120 cm), with a combination of thin first-year (30-70 cm in thickness), grey-white ice (15-30 cm) and grey (10-15 cm) ice, between the end of February and the beginning of March. Although these are general conditions, they provide an estimate of the maximum thickness of the larger floes.

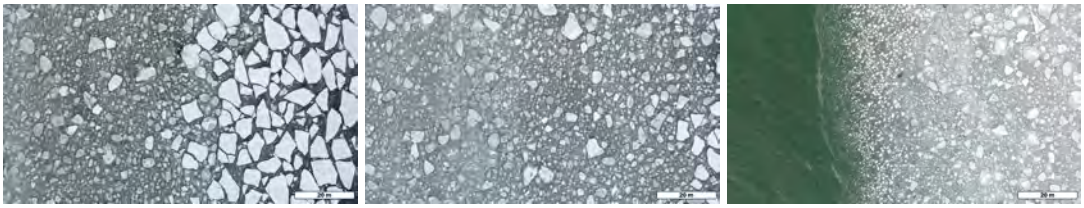

#1 2019-03-05T16:02:13Z #2 2019-03-05 16:04:13Z #3 2019-03-05 16:06:03Z

#4 2019-03-07 16:31:18Z #5 2022-02-20 18:03:34Z #6 2022-02-20 20:58:33Z

#7 2022-02-20 21:52:56Z #8 2022-02-21 16:07:07Z #9 2022-02-21 16:22:07Z

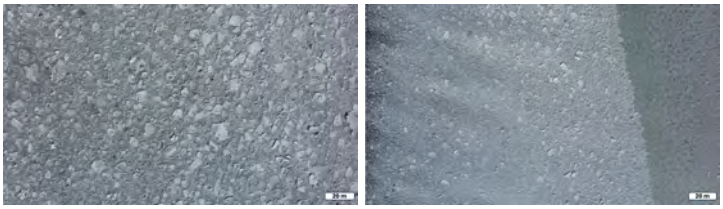

#10 2022-02-21 17:02:58Z #11 2022-02-24 18:52:11Z

Figure 8 – Ice conditions for all eleven (11) events in chronological order, with UTC date and time. Images are oriented so that the ice edge is on the left with waves coming in from the lower left corner.

We can gain a more detailed understanding of our specific ice conditions by examining Figure 8. The previous broad statements reflect our observations: new ice, nilas, pancakes, and brash, which are likely composed of broken pieces of grey-white or thin first-year ice. We observe here small pieces of ice eroded by friction between former larger floes. In most cases, the floes are rounded, which is a sign of advanced erosion. We here use the word

jumble, already mentioned in the previous section, to refer to a pack of stacked, irregular floes formed in rough seas. The dominant floe dimension for all events is ice cake, with a width ranging from 2 m to 20 m.

Some events present unique characteristics distinguishing them from the lot. The videos taken on March 5, 2019, during events #1 and #2, show the largest ice floes, with a maximum estimated caliper size of 12-13 m. These floes with sharper edges appear to be formed by fragmentation caused by wave-induced bending. The floe size distribution (FSD) for events #5 to #10 appears more uniform, with the dominant size being around 5 m to 8 m. The impact of waves at the edge affects the size of ice floes, with smaller ones closer to the edge and larger, sharper ones further into the MIZ. However, events #6 and #7 do not follow this pattern as the videos were taken further into the pack, showing the heterogeneity of the ice in this area. Event #11 also displays non-uniform ice composition, with a strip of nilas or grey ice pancakes clearly appearing further from the edge.

Figure 9 shows an overview of the ice field on February 20 and 24, 2022, highlighting the above-mentioned discrepancy in the FSD and ice composition for events #6, #7 and #11. The observed heterogeneity could be attributed to the significant deformation in the surface motion, a consequence of varying wind conditions, tidal currents and coastal ocean circulation. With a shift and return of westerly winds, more recently formed ice could become trapped between two strips of thicker ice and be compacted onto the shore. This occurrence is not uncommon in the St. Lawrence, as ice can drift over significant distances under continuous winds.

(a) February 20, 2022 (events #6 and #7): facing south-east towards Îlet au Flacon, a band of more eroded floes is surrounded by patches with a bigger FSD.

(b) February 24, 2022 (event #11): facing west-south-west, a band of younger smaller sized floes is extending into the MIZ up to 180 m inwards and is compacted between two strips of ice conditions with different age and size characteristics.

Figure 9 – Larger-scale ice conditions for February 20 and 24, 2022, depicting the heterogeneity of the ice cover for events #6, #7 and #11.

Event #4 also appears to be different from the general conditions of other events. The first visual component is the colour of the thick blueish layer of ice close to the edge. On March 6, 2019, precipitation of snow occurred, leading to this increased presence of wet snow in the water, known as slush and categorized as a type of new ice (WMO, 2014). Slush is different from frazil by its formation process: it comes from solid precipitation in cold water and can solidify, consolidate, thicken and/or form into pancakes under the action of waves. What we see in-between floes for other events appears to be a mix of crushed ice coming from floe-floe collisions, as well as new ice forming in the cold water between the ice pieces.

1.4.2 Dynamical quantities derived from the ice velocity field

In this section we use one particular event to demonstrate how the methodology is applied to extract a viscosity value for the MIZ. The event we chose was filmed on February 20, 2022, at 20:58:33 UTC. From the application of PIV, we obtain the velocity field of the ice $\mathbf{u}$ from which we extract the Cartesian component v, parallel to the ice edge and to the y-axis. We compute the temporal mean over all frames, denoted as $\overline{\mathbf{v}}(x, y)$ and shown in Figure 10.

Note that while the velocity field can be decomposed as mentioned above, we can also obtain a measure for the mean current, i.e. the mean drift speed of the ice over the total duration of the videos, by stating that $U = |\mathbf{u}|$, with the total mean velocity expressed as $U_{\text{mean}} = \langle \overline{U} \rangle_{x,y}$.

(a) Event #1

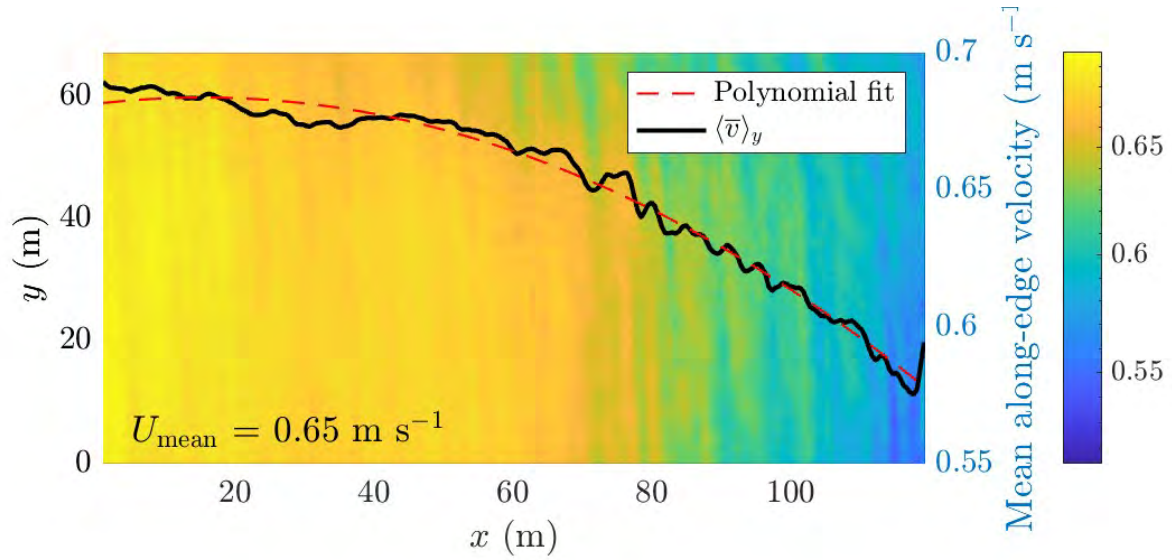

(b) Event #6

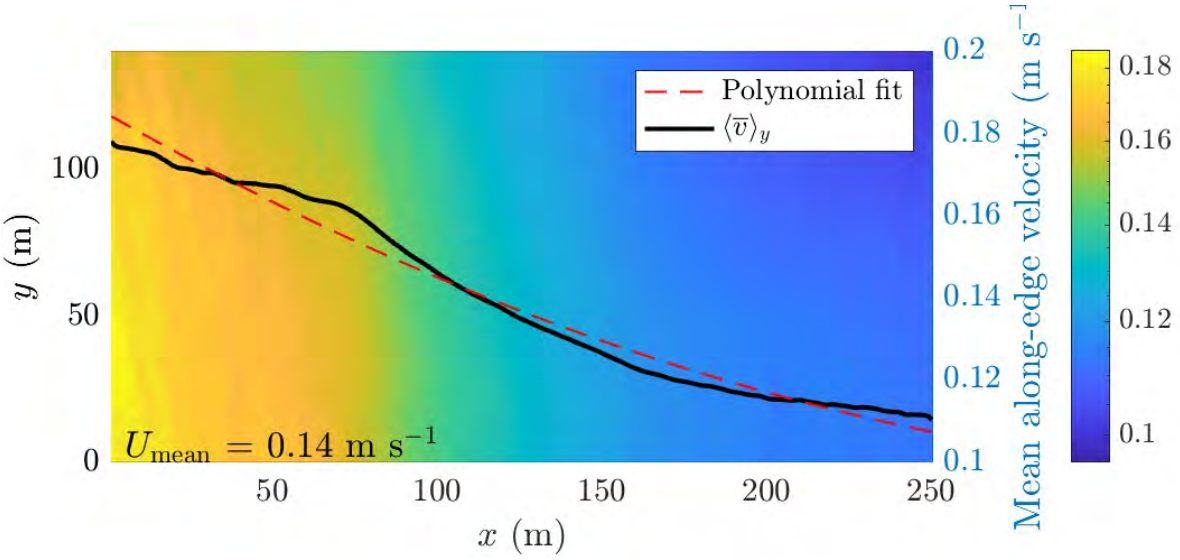

Figure 10 – Spatial distribution of the temporal mean along-edge velocity $\overline{\mathbf{v}}(x, y)$ in m s^{-1} for event #1 and #6. In (a), the mean velocity is decreasing following a second-order polynomial fit, with the shape of an inverted parabola. The total mean velocity (through all frames and in x and y) is 0.65 m s^{-1}. In (b), the mean along-edge velocity is decreasing following an exponential. The total mean velocity is 0.14 m s^{-1}.

Figure 10 illustrates the two most observed behaviors for $\overline{v(x)}$: it decreases with distance from the ice edge following either a quadratic function (negative parabola) or following a decreasing exponential. The curvature of the slope of the velocity decay determines its sign: if the velocity decreases more rapidly further from the edge, the first-order derivative can exhibit an inverted parabolic decay rather than an exponential one. In both cases, the shearing conditions are visually apparent, with velocities closer to the ice edge ($x = 0$) being notably higher and decreasing as distance from the margin increases. The curvature of the mean along-edge velocity component $\frac{\partial^2 \overline{v}}{dx^2}$ is thus obtained analytically from the curve fit, which is displayed in Figure 10. The streaky pattern appears to be associated with the presence of wider floes further from the edge.

Following that $\mathbf{v} = \overline{\mathbf{v}} + \mathbf{v}'$, subtracting the time-averaged velocity from the total velocity field yields the fluctuation velocity, dominated by the surface wave orbital motion, as shown on Figure 11.

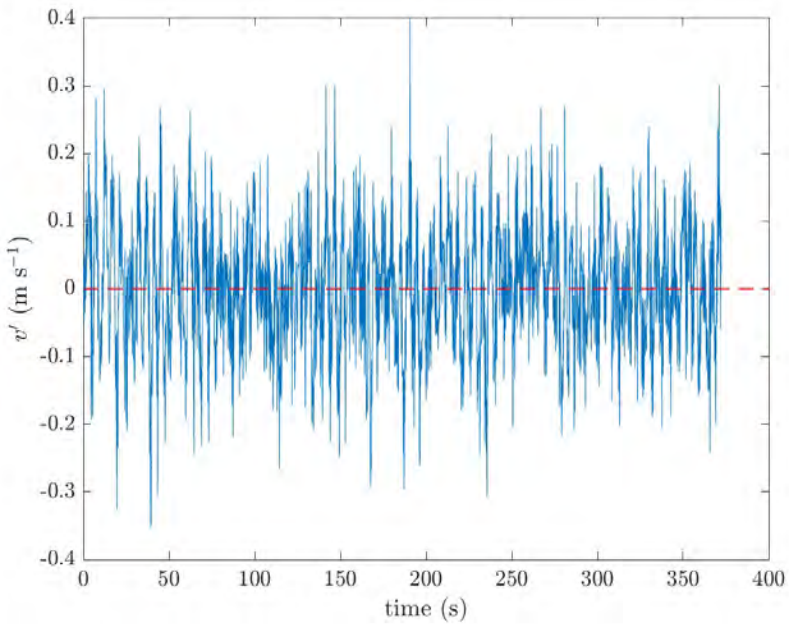

Figure 11 – Temporal variation of the v-component of the orbital velocity for the video duration, in m s^{-1}.

Going forth with the method, from the visual propagation pattern seen in the display of the orbital velocities, we can geometrically extract the value of the wave direction, as seen on Figure 12. An average over multiples values on multiple frames (around 30 measures per event) led to the extraction of θ, with an error of $\pm$ 1° for all events except event #4 with 2° uncertainty.

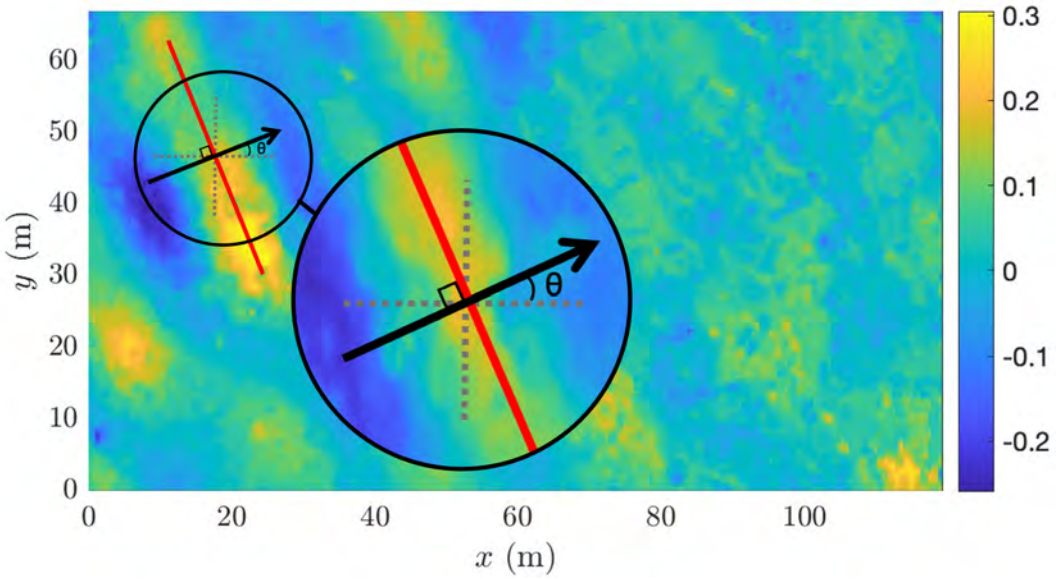

Figure 12 – Spatial distribution of the v-component of the orbital velocity in m s^{-1} (colorscale) for the first frame, with the geometric decomposition of the angle of incidence θ, for event #1.

It is also possible to quantify the wave energy with these values of orbital velocity by applying the Welch method for a spectral analysis with a Hanning window and a sampling frequency of 5 Hz. The signal is sliced into three sections and a discrete Fourier transform is applied with frequency ranging from approximately 0.2 to 0.5 Hz. The result of this data manipulation is the surface orbital velocity variance spectrum. The following calculations are made to characterize the wave train for each event and are derived from the wave linear theory (Ardhuin and Filipot, 2016). The surface orbital velocity variance can be transformed into an amplitude variance spectrum with a factor of frequency $(2\pi f)^2$, with a mean shape (averaged for all points) seen on Figure 13.

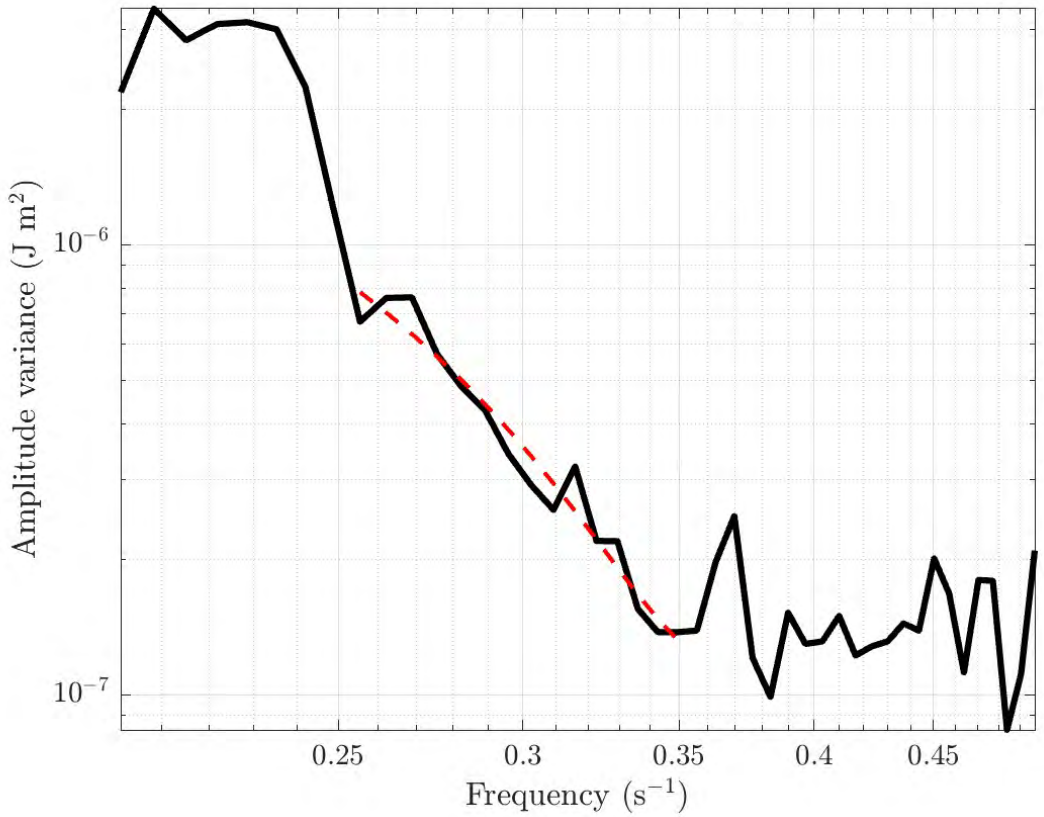

Figure 13 – Averaged shape of the amplitude variance spectrum for event #6, for frequencies between 0.2 and 0.5 Hz.

Do note that here we use the variance of amplitude for the quantification of energy attenuation, keeping in mind that the constants conversing amplitude to energy (ρg) appear in our final equation 1.15. From here, we can use the moments of the spectrum, defined as

$$m_n = \int_0^\infty f^n E(f) df, \tag{1.18}$$

to estimate the mean period T_m and the significant height H_s. For this, we use

$$H_s = 4\sqrt{\int_0^\infty E(f) df} = 4\sqrt{m_0} \tag{1.19}$$

and

$$T_{m_{0,n}} = \left(\frac{m_n}{m_0}\right)^{-\frac{1}{n}} \Rightarrow T_{m_{0,2}} = \sqrt{\frac{m_0}{m_2}}. \tag{1.20}$$

$T_{m_{0,2}}$ is very close to a wave-by-wave mean period, which is influenced by the choice of the maximum frequency. Results for all dynamic relevant parameters described here are shown in Table 3. By integrating the amplitude variance spectrum over all frequencies, we can also extract the total variance for a single point and extend it to a spatial distribution.

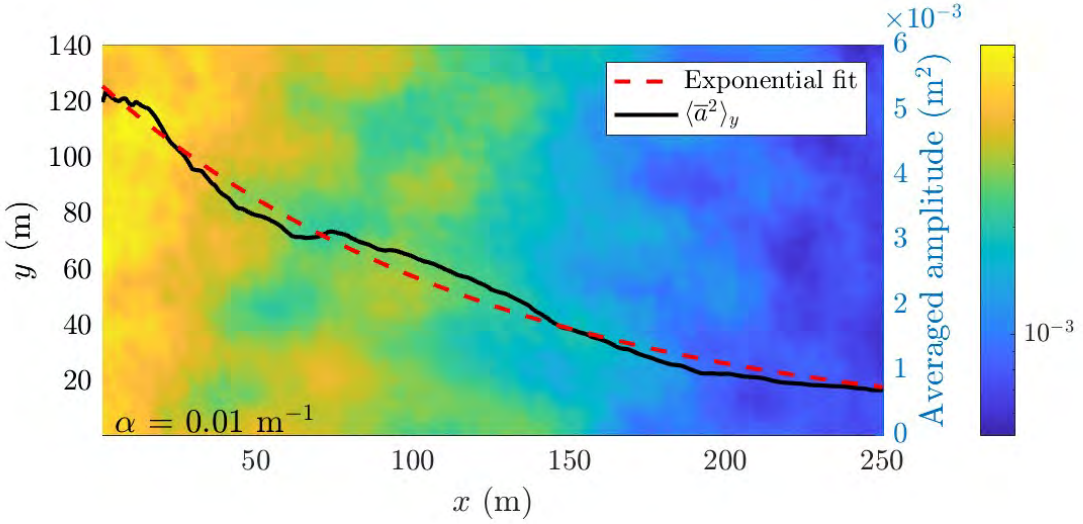

Figure 14 – Spatial distribution of the total wave amplitude variance $E(x, y)$ (colorscale), superimposed with the along-edge average $E(x)$ (black line) and the exponential fit (red line), in m^2, for event #6.

Given that the energy decay follows an exponential form as shown in equation 1.17, we can compute a polynomial fit to the averaged amplitude over the propagation direction and extract its derivative, leading to the second missing term $\frac{\partial E}{\partial x}$. An additional step was added to take into account the boundary effect of the edge in some cases. For events #3, 4, 5, 8, 9 and 11, we resized along the x-axis to exclude the region where waves are propagating in an ice concentration below 15% (see Figure 8). The corrected frames don't include wave detection and velocity in the water, where the displacement caused by the waves' movement is significantly greater than in the ice. The first 20, 60, 75 and 120 m were respectively

masked for events #11, #3-4, #5-9 and #8. By combining the results for the second-order derivative for the mean along-edge velocity, the angle of incidence and the attenuation of the amplitude variance in the pack, we reach the final step of the method and use equation 1.15 to calculate the value of the shear viscosity. For this example presented as event #6, the shear viscosity has an absolute value of 3.7 $(1.1, 8.5) \times 10^3$ kg s^{-1}, with the numbers in parenthesis showing the minimum and maximum values considering the various uncertainties.

Table 3 presents the estimates for the main physical quantities measured, for all eleven events.

Table 3 – Estimates of relevant physical quantities for the selected events. The first column represents the space and time average velocity, θ is the angle of incidence of the waves, $\overline{H_s}$ is the mean significant wave height, $\overline{T}$ the mean wave period, $\left\langle \frac{\partial E}{\partial x} \right\rangle$ is the wave energy attenuation along the x-axis, $\tilde{\alpha}$ and α are the wave energy attenuation coefficients along the x-axis and along the direction of propagation, respectively, $\frac{\partial^2 v}{\partial x^2}$ is the second-order derivative of the mean along-edge velocity, $|\dot{\varepsilon}_{12}|$ is the deformation rate (shear rate) module and finally $\langle \eta \rangle$ is the mean shear viscosity.

Event	$\langle \overline{U} \rangle_{x,y}$	θ	$\overline{H_s}$	$\overline{T}$	$\left\langle \frac{\partial E}{\partial x} \right\rangle$	$\tilde{\alpha}$	α	$\frac{\partial^2 v}{\partial x^2}$	$\lvert\dot{\varepsilon}_{12}\rvert$	$\langle \eta \rangle$
	m s^{-1}	°	m	s	10^{-4} m	10^{-2} m^{-1}	10^{-2} m^{-1}	m^{-1} s^{-1}	10^{-3} s^{-1}	kg s^{-1}
1	0.654	22	0.174	3.35	−0.180	0.978	1.055	-2.02×10^{-5}	0.433	-
2	0.698	23	0.207	3.23	−0.175	0.800	0.869	-1.41×10^{-5}	0.347	-
3	0.735	25	0.303	2.93	−0.201	0.361	0.398	8.75×10^{-5}	0.057	4.4×10^{2}
4	1.193	35	0.873	4.01	−0.281	0.075	0.091	-6.52×10^{-5}	0.084	-
5	0.362	43	0.406	3.87	−0.374	0.484	0.662	-1.45×10^{-5}	0.453	-
6	0.142	44	0.204	4.08	−0.187	0.800	1.112	1.26×10^{-6}	0.155	3.7×10^{4}
7	0.083	47	0.211	3.71	−0.545	1.532	2.246	7.38×10^{-6}	0.331	1.9×10^{4}
8	0.489	29	0.680	4.10	−0.727	0.326	0.372	-2.06×10^{-5}	0.712	-
9	0.421	27	0.561	4.35	−0.704	0.606	0.681	-1.55×10^{-5}	1.300	-
10	0.213	29	0.208	3.79	−0.122	0.614	0.703	7.70×10^{-6}	0.568	3.4×10^{3}
11	0.636	48	0.512	4.00	−1.780	1.131	1.690	-5.24×10^{-6}	0.444	-

Looking at Table 3, one noticeable characteristic affecting the shear viscosity is the

variability in the second-order derivative's sign for the average velocity along the edge $\frac{\partial^2 \overline{v}}{\partial x^2}$. Fundamentally, viscosity has a positive value. As stated before, the variation in the curvature of the velocity profile determines the sign of viscosity: if the velocity decreases more rapidly further from the edge, the second-order derivative can exhibit an inverted parabolic decay rather than an exponential one (see Figure 10a). Seven of the eleven events present a negative value for the derivative, hence a negative value for the shear viscosity. For these events, the shear viscosity was not incorporated in the results since the model developed was deemed not valid.

With that being said, the model is applicable only to the quantification of the shear viscosity: the other ancillary results, such as the amplitude variance and velocity field, are measured simply from the videos using the PIV. While bearing negative viscosity, nine events showed an exponential decay of energy, with four of those showing significant noise further from the edge. For the mean along-edge velocity, nine events also showed a decrease in respect with x, but only three with a negative curvature. The next sections discuss those intermediate findings.

Event #4

As mentioned previously in section 1.4.1, ice conditions for event #4 differ from other events, in part due to a heavy snowfall in the days preceding the capture of the video. The estimated 30 cm young ice pancakes forming at the ice edge appear to be surrounded by a denser layer of new ice, mainly slush and shuga, that extends towards the MIZ's interior. Examining more carefully Figure 8 for event #4, certain pancakes near the edge appear to align in bands in the direction of wave propagation, suggesting movement in the x direction and thus contradicting one of our three main assumptions. The analysis of the edge displacement over the course of the video confirmed an approximate shift of the edge 32 m inwards into the MIZ.

This event yields the highest mean velocity at 1.193 m s^{-1}, the highest significant wave height at 0.873 m and the smallest attenuation coefficient at 0.075×10^{-2} m^{-1}. In this mix of newly formed ice and slush near the edge, velocity values are comparable to those in water. This similarity is shown in Figure 15 and emphasizes the possible importance of younger non-consolidated ice and its ability to transfer or hinder momentum amongst floes, which may have been disregarded in our simplified MIZ idealization. This is separate from conditions during event #3, taking place two days earlier, where the ice resembles more the jumble definition presented in section 1.4.1, i.e. small scattered eroded floes.

The alignment of the thicker floes with the propagation is also resulting in a different pattern for the attenuation of energy, leading to a variation in total amplitude that deviates from the expected exponential decay. While we are looking at the apparent attenuation along the x-axis, we can still see a variance discrepancy aligned in the direction of propagation, unseen in other events. A similar trend is visible in the mean along-edge velocity, where velocity increases between 50 m and 80 m. One of the plausible explanation for this phenomenon would be refraction due to the heterogeneity of the floes.

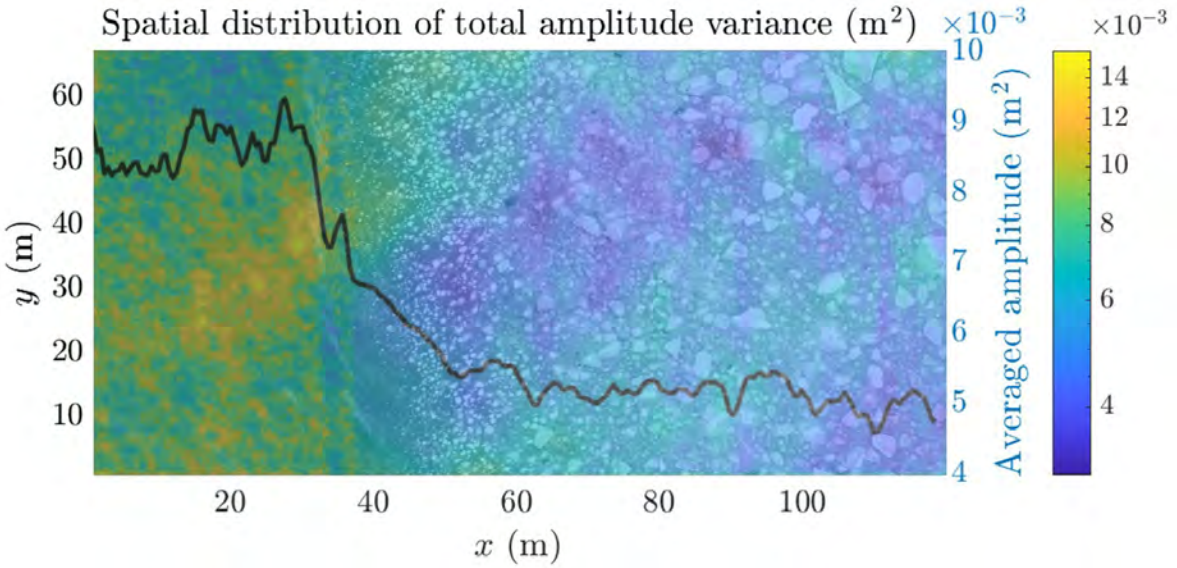

(a) Event #3: the first 40 m of the frame is mainly open water, which affect the amplitude variance measured. A decrease in amplitude variance is visible as soon as the wave enter the ice jumble around x=40 m.

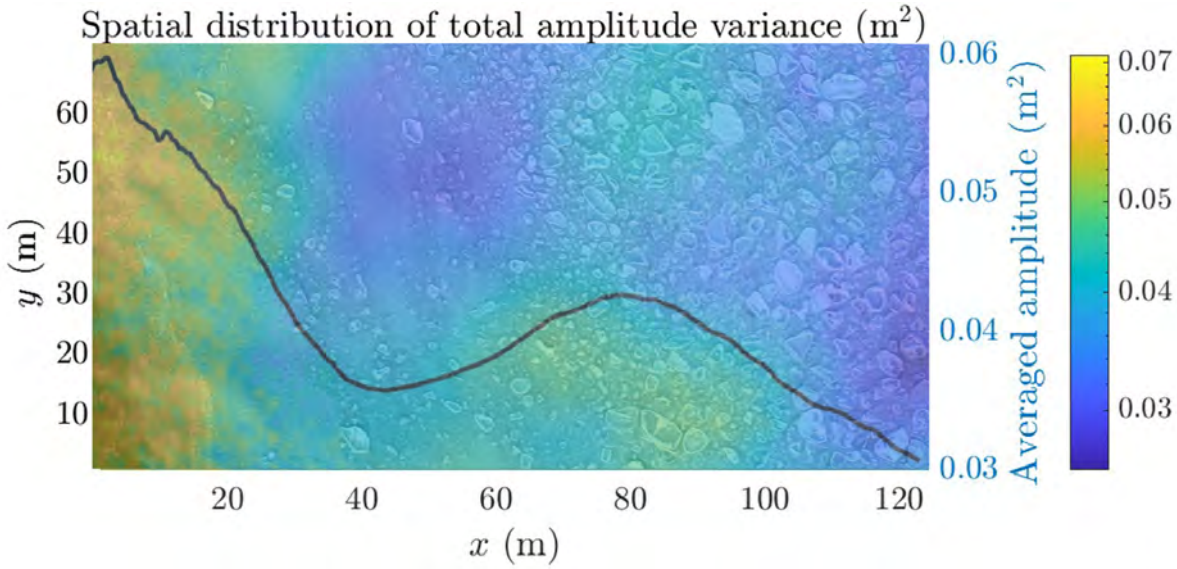

(b) Event #4: the average amplitude follows a declining trend in accordance with a strip of thicker floes aligned in the direction of propagation up to x = 40 m. The heterogeneity of the ice between x = 40 m and x = 80 m leads to an unexpected trend in the wave energy attenuation.

Figure 15 – Comparison of spatial distributions of total amplitude variance for event #3 and #4: the patchy detection of amplitude in the water (40 first meters of event #3) is similar to the mix of new ice (20 first meters of event #4).

Events #6, #7 and #10

Three of the four events showing a positive viscosity also exhibit a clear correlation between the mean velocity and the energy decay: event #6, #7, and #10. Figure 16 displays the spatial distributions of total amplitude variance and mean along-edge velocity for events #7 and 10 (see section 1.4.2 for event #6).

(a) Event 7 - 2022/02/20 21:52:56Z

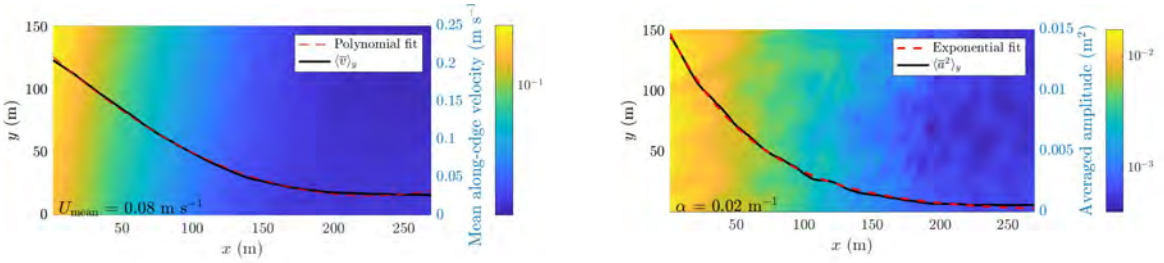

(b) Event 10 - 2022/02/21 17:02:58Z

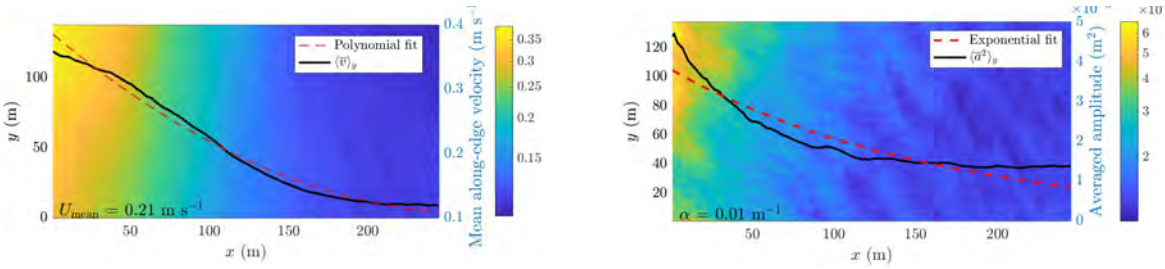

Figure 16 – Spatial distributions of the along-edge velocity $\overline{v}$ and of the total wave amplitude variance $E(x, y)$ (colorscale), superimposed with the along-edge averages (black line) and respective polynomial and exponential fits (red line) for 2 selected events (#7, 10).

The average energy along the x-axis demonstrates exponential decay in accordance with the Airy ansatz. These three events were filmed further into the MIZ and possess a more uniform FSD. In the ice jumble, we see well eroded floes with raised edges from collision and friction with the surrounding pack. These are encircled within a mixture of crushed small

pieces and shuga/slush as a result from said erosion. Event #7 shows the most accurate fit for mean velocity and total amplitude variance, with respective standard deviations of residuals of 1.98×10^{-3} m s^{-1} and 1.42×10^{-4} m^2.

Event #3

It was previously mentioned that four events led to the result of a positive viscosity and that the sign of the double derivative of $\overline{v}$ was responsible for the variation in sign of η. While this is true for event #3, we consider that the model doesn't apply to this event. The velocity field appears to be increasing in distance from the edge, as illustrated on Figure 17.

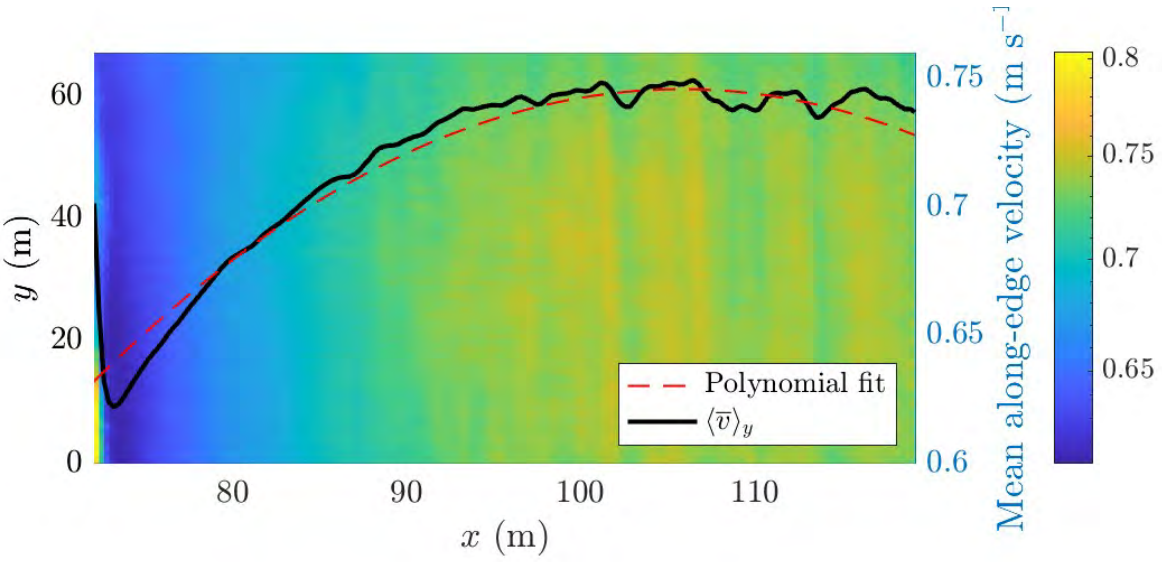

Figure 17 – Spatial distribution of the temporal mean along-edge velocity $\overline{v}$ in m s^{-1} for event #3, where we see an upward trend with distance to the edge.

This is an unexpected behaviour for the velocity: if the energy is declining, which it is for this event, we do not have the additional data to determine what factor is making the velocity increase with distance from the edge.

1.4.3 Shear viscosity

Figure 18 shows shear viscosity values (red dots) computed using equation 1.15 with dynamical quantities derived from the ice velocity fields of events #6, #7 and #10 presented in the previous sections. The error bars depict the uncertainty interval for each input parameter. In order to interpret these data, we compare them to the viscous-plastic model of Hibler (1979) (H79), which is the most widely used in climate studies as well as for short-term forecasting applications. This model implies that the shear viscosity is proportional to the compressive strength P of the ice and to a function of the strain rate, such that

$$\eta = \frac{P}{f(\dot{\varepsilon}_{ij})} \tag{1.21}$$

where

$$f(\dot{\varepsilon}_{ij}) = 2e^2 \left[\left(\dot{\varepsilon}_{11}^2 + \dot{\varepsilon}_{22}^2 \right) \left(1 + e^{-2} \right) + 4e^{-2} \dot{\varepsilon}_{12}^2 + 2\dot{\varepsilon}_{11}\dot{\varepsilon}_{22} \left(1 - e^{-2} \right) \right]^{\frac{1}{2}} . \tag{1.22}$$

This function describes an ellipse in the principal strain rate plane with a major-to-minor axis ratio e. In the simple case where $\dot{\varepsilon}_{11} = \dot{\varepsilon}_{22} = 0$, $f(\dot{\varepsilon}_{ij})$ reduces to $4e\dot{\varepsilon}_{12}$. The parameter P determines the dependence on ice parameters. Two formulations are considered here. Hibler's model, noted P_{H79}, has a linear dependence on ice thickness h while the model of Uzuner and Kennedy (1976), noted P_{UK76} has a quadratic dependence on h. For compact ice, i.e. for a 100% concentration,

$$P_{\mathrm{H79}} = P^* h \tag{1.23}$$

$$P_{\mathrm{UK76}} = K_r h^2 \tag{1.24}$$

where P^* is an adjustable constant and

$$K_r = \frac{\rho g}{2} \left(1 - \frac{\rho}{\rho_w} \right) (1 - n) \left(\frac{1 + \sin\phi}{1 - \sin\phi} \right). \tag{1.25}$$

The UK76 model has been derived for an ice jumble made of small ice floes piled up on each other, with a porosity n and an internal friction angle ϕ, representative of river ice jams. It has been applied and validated with in situ data by Sutherland and Dumont (2018) for very similar marginal ice zone conditions and at the same site as the results presented in this work.

These results not only compare the observations with the models, but also illustrates that the widely used Hibler's rheology is not representative of our idealized MIZ. The granular theory seems to be more in accordance with the results, still keeping in mind that the shear viscosities obtained are on the lower side of the range. We can also note a similar dependence of the shear viscosity with the shear rate as in the models.

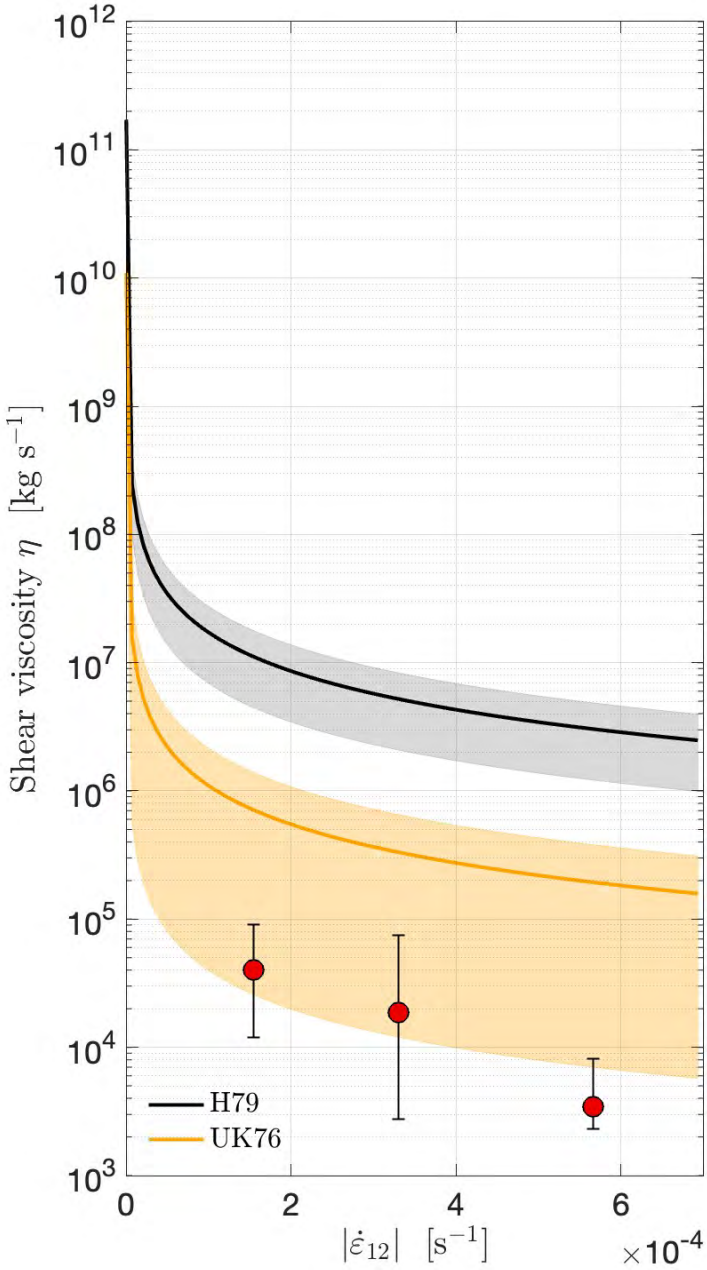

Figure 18 – Shear viscosity values estimated using equation 1.15 for events #6, #7 and #10 (red dots from left to right) superimposed with the prediction of the viscous-plastic rheology of Hibler (1979) (H79, black) and the Mohr-Coulomb rheology of Uzuner and Kennedy (1976) (UK76, yellow) for a range of possible parameter values (h = [0.2, 0.8] m, e = 2.0, P^* = 2.75 × 10^4 Pa, n = [0.3, 0.5] and ϕ = [26, 58]°.

1.5 Discussion

With the use of aerial imagery in the St. Lawrence Estuary, we measured the mean velocity field, extracted the orbital wave velocity, measured the angle of incidence of the wave train and estimated the wave propagation and energy attenuation within the ice field. The shear viscosity was quantified in four high resolution (width between 150 m and 270 m) events for the MIZ and three of those were compared to Hibler's rheology and Mohr-Coulomb granular theory. The following discussion is examining the validity of the assumptions that led to the formulation of the model 1.15 for the shear viscosity and its applicability to the data.

First, the main assumption made in the development of equation 1.15 was that the viscosity is constant within the frame of our MIZ. Let's recall equation 1.11, which is a balance between the diagonal term of the wave radiative stress and the diagonal term of the Cauchy tensor

$$\tau_{wy} = \frac{\partial}{\partial x}\left(\eta \frac{\partial v}{\partial x}\right) \tag{1.26}$$

and can be further developed as

$$\begin{aligned} \tau_{wy} - \frac{\partial \eta}{\partial x}\frac{\partial \overline{v}}{\partial x} \quad &- \eta \frac{\partial^2 \overline{v}}{\partial x^2} = 0 \\ (1) - (2) \qquad &- (3) = 0. \end{aligned} \tag{1.27}$$

By assuming that the derivative of η along x is null, hence that term (2) in equation 1.27 is null, we obtained equation 1.15 for the modelled shear viscosity. If we assume however that η is not constant through the pack, i.e. that its derivative along x is not zero, we need to consider that the term (2) could be dominant. We know that term (1) is negative (since it is proportional to $\partial E/\partial x$), that η is positive, and that the mean along-edge velocity is expected to decrease with x ($\partial \overline{v}/\partial x < 0$). As we saw in section 1.4.2, the derivative of the velocity could be positive, but we expect that, with the conditions developed for the applicability of the model, the velocity should decrease with the distance into the ice field since there is

an energy decay. Our results also show that, in some cases, term (3) can be negative (see section 1.4.2 and Table 3), which leaves us with two options. If term (3) is positive, we can't draw any conclusion on the sign of term (2) since it could be null and equation 1.27 could still be satisfied. But if term (3) is negative, term (2) needs to be positive in order to balance the equation where the sum of the three terms equals zero. With (2) being positive and assuming that $\overline{v}$ decreases with x, the derivative of η along x must be negative, meaning that the viscosity decreases with respect to the edge.

Based on data from Sutherland and Dumont (2018), we can infer that thickness increases from the ice edge following a function of type $1 - e^{x/l_h}$, where l_h is the characteristic thickening length scale. If we assume that viscosity increases with thickness, it would therefore increase with distance from the ice edge, not decrease. On the other hand, viscosity can also vary with wave agitation, which decreases with distance. And if wave agitation increases viscosity (increasing momentum transfer efficiency), viscosity decreases with distance. To correctly inform these additional hypotheses, more detailed observations of the ice characteristics across the MIZ are required.

In the present work, we will only give a brief overview of that variation of η. Assuming that the viscosity is not a constant also leads to the possibility of quantifying its variation within the MIZ. Equation 1.15 implies that we average values for the amplitude variance in x and y to obtain one singular value. Figure 19 illustrates the variation of the viscosity along the x-axis, if we do not perform the additional averaging step.

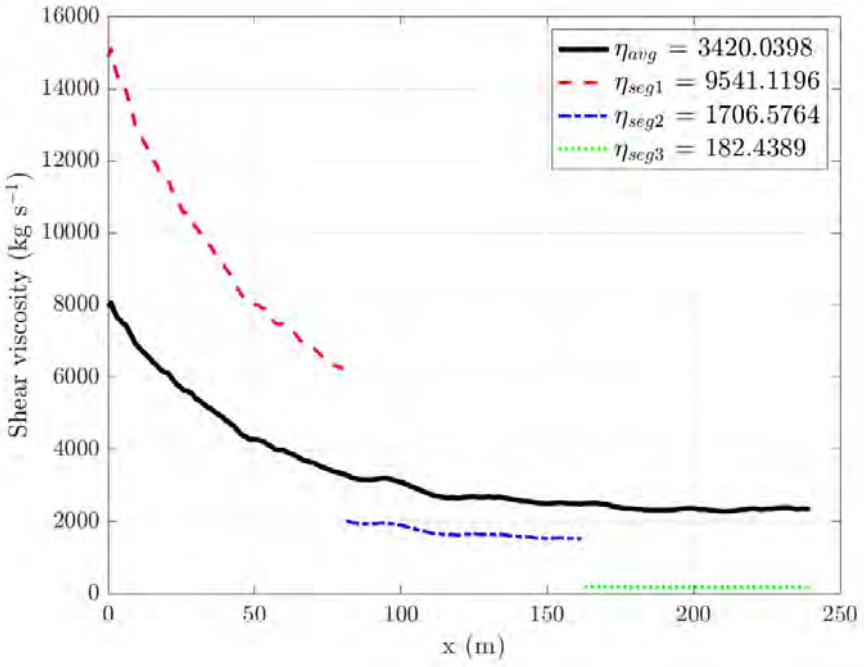

Figure 19 – Shear viscosity variation for event #10. The black curve represents the variation of η along the x-axis, while the three other curves have been obtained and calculated for three windows on the image: window 1 covers the first 80 m, window 2 is for $x \in [81, 161]$ m and window 3 for $x \in [162, 242]$ m.

Figure 19 illustrates that the viscosity is decreasing with respect to x for event #10, with the strongest slope in the first window. In window 3, the furthest from the edge, the shear viscosity is almost constant. This exercise was also done for events #6 and #7, yielding the same declining trend with respect to the distance from the margin.

With a purely analytical approach, if we consider that $\eta(x)$, the y-component of equation 1.14 needs to be developed as the derivative of a product such that

$$\rho_w g \frac{\partial E}{\partial x}\left(\frac{1}{2}\cos\theta\sin\theta\right) + \frac{\partial \eta}{\partial x}\frac{\partial v}{\partial x} + \eta\frac{\partial^2 v}{\partial x^2} = 0. \tag{1.28}$$

This can be rewritten as the a first-order linear differential equation

$$\frac{\partial \eta}{\partial x} + p(x)\,\eta = q(x) \tag{1.29}$$

with

$$\begin{aligned} p(x) &= \frac{\partial^2 v}{\partial x^2}\left(\frac{\partial v}{\partial x}\right)^{-1} \\ q(x) &= -\frac{1}{2}\rho_w g \cos\theta \sin\theta \frac{\partial E}{\partial x}\left(\frac{\partial v}{\partial x}\right)^{-1}. \end{aligned} \tag{1.30}$$

To solve this equation, we multiply equation 1.30 by the function $\mu(x) = e^{\int p(x)dx}$, yielding

$$\mu(x)\,\frac{\partial \eta}{\partial x} + \mu(x)\,p(x)\,\eta = \mu(x)\,q(x). \tag{1.31}$$

Knowing that

$$\frac{\partial \mu}{\partial x} = \mu p, \tag{1.32}$$

we can rewrite the left term as a derivative of products and obtain

$$\frac{\partial}{\partial x}(\mu\eta) = \mu q. \tag{1.33}$$

Integrating over x and isolating η leads to

$$\eta = \frac{1}{\mu}\int \mu q(x) dx \tag{1.34}$$

The final consists in integrating $p(x)$, which is easily done with the following change of variables

$$\begin{aligned} u &= \frac{\partial v}{\partial x} \\ du &= \frac{\partial^2 v}{\partial x^2} dx \end{aligned} \tag{1.35}$$

leading to

$$\int p(x)dx = \int \frac{1}{u}\,du = \ln\left(\frac{\partial v}{\partial x}\right) + C \tag{1.36}$$

and

$$\mu(x) = e^{[\ln(\frac{\partial v}{\partial x})+C]} = C_* \frac{\partial v}{\partial x}. \tag{1.37}$$

Injecting these results in equation 1.34, we obtain an alternative formulation for the shear viscosity with a dependence to x expressed as

$$\eta(x) = C_* \left(\frac{\partial v}{\partial x}\right)^{-1} \left[-\frac{1}{2}\rho_w g \cos\theta \sin\theta \, E_(x) + C_+\right]. \tag{1.38}$$

As the viscosity is defined strictly as the stress-to-strain rate ratio, then C_*, which is an adimensional constant, is equal to 1 ($C = 0$). C_+ on the other hand represents a homogeneous stress (kg s^{-2}) that would apply everywhere (supposed zero in our case), $E(x)$ is the total wave energy profile across the MIZ and $\frac{\partial v}{\partial x}$ is the first derivative of the velocity, which also corresponds in our idealized case to the shear rate $\dot{\varepsilon}_{21}$.

A numerical approach could also be applied to obtain the solution of equation 1.29 by multiplying the polynomial fit for the velocity and energy derivatives.

The optimization of this analysis could also be included in future work, with Dumont (2022) highlighting the potential of discrete element modelling for the derivation of MIZ rheology. By reapplying the method with equation 1.38, we would hope for valid values of shear viscosity for most of the events, but said work is currently outside the scope of this master.

Secondly, we assumed a 2D layer of ice, uniform along z. During ice canoe trips in the BicWin campaigns, piles of two or more floes rafted on one another were often observed. Slush was measured to be up to 80 cm thick and in 2023, along the bank, it was observed to be over 2 m. We here propose that there may be notable variations in shuga or slush thickness, as well as in ice composition (rafting, floe size), that are not visible when observed from the air. There is also a possibility that the motion detected at the surface is different from the motion in and at the base of the ice, i.e. that there could very well be undetected vertical shear in the ice.

Third, we considered that current is negligible in the sense that it is homogeneous over the scale of the imagery captured. While Sutherland and Dumont (2018) explain why that assumption is valid, what we might have failed to account for in this study is the forcing of the waves on the underlying layer of water below the ice and its feedback on the displacement of ice floes. Furthermore, for wave trains submitted to low attenuation, the radiative stress would also be expected to stay on the lower side, hence the hypothesis that it dominates in the MIZ might not hold anymore and could potentially explain some of the issues presented.

Fourth, the wave spectrum obtained was integrated over frequencies ranging from 0.2 Hz to 0.5 Hz to filter some of the noise seen in the averaged shape of the total variance. According to Emmanuel et al. (2022), the role of non-linear wave–wave interactions can be important in shaping the wave spectrum, and we might add to that the floe-floe interactions. This noise in the spectrum could be due to experimental set-up (length of the videos less than 10 min) or material properties (interactions). The use of wave buoys could help quantify more accurately the wave spectrum. Another way to improve the quantification of the wave radiative stress would be through stereoscopy. The deployment of two drones filming the same scene at a pitch angle under 90° could lead to the direct measure of sea elevation.

In order to continue this work, a few point should be addressed to solidify and refine the developed method, such as:

— Considering that the shear viscosity is not constant along the x-axis, as previously detailed by equations 1.28 to 1.38;
— Measuring the currents at the survey site with buoys: Sutherland et al. (2018) discusses the forcing from tidal currents in greater details, but specific measurements for the dataset presented in this thesis would be optimal;
— Fitting a slope over the energy variance spectrum between an acceptable range of frequencies, such as 0.25 Hz to 0.35 Hz, and a subsequently extrapolating the values outside this bracket to limit the noise seen in multiple events;
— A more thorough examination of the calibration and distortion effects in the videos: the

automatic distortion correction of the DJI Mavic 2 Pro Drone was used, but a more in-depth analysis could be done to minimize and suppress the small movements from one frame to the other;

— Correlating the viscosity values obtained with other rheologic parameters, such as ice thickness and floe size distribution;

— Apply the method to other MIZ in different environments, like in the Arctic, in order to compare and unify the rheological properties of all MIZ.

1.6 Conclusion

The main objective of the present study was to contribute to a better understanding of MIZ dynamics, recognizing its growing importance in the Arctic sea ice pack with recent acceleration of climate changes. Based on the work of Sutherland and Dumont (2018), we deployed an UAV at the ice edge in BdHH multiple times from March 2019 to February 2022. A selection of eleven events of oblique wave propagation near the ice margin were filmed and studied to simultaneously measure the wave radiative stress and the associated shear deformation. By extracting the mean velocity field with PIV, we obtained estimates for physical properties specific to each event, such as the mean displacement, the angle of incidence of waves, the mean period, the significant wave height, the attenuation coefficient, the derivative of the along-edge velocity (indicative of shear), the deformation rate and the shear viscosity. Attenuation coefficient in the order of 10^{-2} m^{-1}, significant height below 1 m and mean period around 3 s to 4 s are within the expected range for waves around BdHH (previously observed during the BicWin winters). An exponential wave attenuation following the Airy ansatz was present in nine events, sometimes only partially due to noise impacting the amplitude variance further into the pack. The two other events presented significant noise along the variance spectrum.

The model developed considered an idealized MIZ and was based on three main assumptions: a stationary ice edge, the variation along the y-axis is zero and the shear viscosity

doesn't vary significantly on the considered spatial scale. Out of the eleven datasets, the model developed was deemed applicable to three events (# 6, 7, 10). The other eight returned negative values for η or an increase in velocity with respect to the distance with the edge, and thus did not fit into the developed conceptual framework. The three values obtained were compared to Hibler viscous-plastic and Mohr-Coulomb granular rheologies, respectively. The measured shear viscosity values are in the order of $10^3 - 10^4$ kg s^{-1}. These values agree best with the granular theory, suggesting that the widely used rheology of Hibler is not suitable for observations made in the MIZ.

The assumption that the shear viscosity is constant is seen as the main one to relax in future work, since the derivative of η along the x-axis vary at least one order of magnitude within the ice field, even with a fine spatial scale between 180 m to 270 m. Assessing the shear viscosity values would then require solving a differential equation, instead of a simple algebraic equation. The role of floe-floe interactions, the non-uniform sea ice thickness distribution and the feedback of wave propagation in the underlying water layer of the ice cover are also additional sources of uncertainty.

CONCLUSION GÉNÉRALE

L'objectif principal de la présente étude était de contribuer à une meilleure compréhension de la dynamique de la MIZ, un besoin basé sur de récentes études (Aksenov et al., 2017; Boutin et al., 2020) soulignant son importance accrue dans la banquise Arctique avec l'accélération des tendances climatiques. Sur la base des travaux de Sutherland and Dumont (2018), de multiples vols de drone ont été effectués à la lisière de glace dans la BdHH, échelonnés sur plusieurs campagnes de terrain de mars 2019 à février 2022. Une sélection de onze événements capturant la propagation de vagues à incidence oblique à la marge de glace a été étudiée pour mesurer simultanément la contrainte radiative des vagues et la déformation en cisaillement associée. En extrayant le champ de vitesse moyen à l'aide de la PIV, nous avons obtenu des estimations pour neuf propriétés physiques spécifiques à chaque événement, telles que le déplacement moyen, l'angle d'incidence des vagues, la période moyenne, la hauteur significative, le coefficient d'atténuation, la dérivée de la composante de la vitesse parallèle à la marge (indicative du cisaillement), le taux de déformation et la viscosité de cisaillement. Un coefficient d'atténuation de l'ordre de 10^{-2} m^{-1}, une hauteur significative inférieure à 1 m et une période moyenne de 3 s à 4 s se situent dans l'intervalle attendu pour les trains de vagues habituels à l'intérieur de la BdHH (observée précédemment durant les campagnes BicWin). Une atténuation exponentielle des vagues suivant l'ansatz d'Airy était présente dans neuf événements, parfois seulement partiellement en raison du bruit affectant la variance de l'amplitude plus loin dans la banquise.

Le modèle développé considère une MIZ idéalisée et est basé sur trois hypothèses principales : une marge stationnaire, des variations en y nulles et une viscosité de cisaillement constante, c'est-à-dire qui ne varie pas de manière significative sur l'échelle spatiale considérée. Sur les onze ensembles de données sélectionnés, le modèle développé a été jugé applicable à trois événements (# 6, 7, 10). Les évènements restants ont mené à des valeurs négatives pour η ou à une augmentation de la vitesse en fonction de la distance avec la marge,

ne correspondant ainsi donc pas au cadre conceptuel proposé. Les trois valeurs positives obtenues ont été comparées à la rhéologie visco-plastique d'Hibler et la théorie granulaire Mohr-Coulomb. Les viscosités mesurées possèdent un ordre de grandeur entre 10^3 et 10^4 kg s^{-1}. Ces valeurs s'alignent plus conformément avec le modèle granulaire, suggérant que la rhéologie d'Hibler, largement utilisée dans les modèles globaux de prédiction de glace, n'est pas adaptée aux observations tirées de la MIZ.

L'hypothèse principale d'une viscosité de cisaillement constante a été suggérée comme le point principal à développer dans les travaux futurs puisque la dérivée de η le long de l'axe x s'est avérée varier d'au moins un ordre de grandeur dans le couvert glaciel, malgré une échelle spatiale entre 180 m et 270 m. Le rôle des interactions floe-floe et/ou vague-vague, la distribution non-uniforme de l'épaisseur de la glace de mer et la rétroaction de la propagation des vagues dans la couche d'eau sous-jacente à la couverture de glace ont également été évoqués comme possibles améliorations dans la paramétrisation du modèle d'équilibre présenté.

RÉFÉRENCES

Aksenov, Y., Popova, E. E., Yool, A., Nurser, A. J., Williams, T. D., Bertino, L., and Bergh, J. (2017). On the future navigability of arctic sea routes: High-resolution projections of the arctic ocean and sea ice. *Mar. Pol.*, 75.

Ardhuin, F., Collard, F., Chapron, B., Girard-Ardhuin, F., Guitton, G., Mouche, A., and Stopa, J. E. (2015). Estimates of ocean wave heights and attenuation in sea ice using the sar wave mode on sentinel-1a. *Geophys. Res. Lett.*, 42.

Ardhuin, F. and Filipot, J.-F. (2016). Ocean waves in geosciences. *Laboratoire d'Océanographie Physique et Spatiale, Brest, France*.

Asplin, M. G., Galley, R., Barber, D. G., and Prinsenberg, S. (2012). Fracture of summer perennial sea ice by ocean swell as a result of arctic storms. *J. Geophys. Res.*, 117.

Belter, H., Krumpen, T., Hendricks, S., Hoelemann, J., Janout, M. A., Ricker, R., and Haas, C. (2020). Satellite-based sea ice thickness changes in the laptev sea from 2002 to 2017: Comparison to mooring observations. *Cryosph.*, 14.

Bennetts, L. G., Bitz, C. M., Feltham, D. L., Kohout, A. L., and Meylan, M. H. (2022). Theory, modelling and observations of marginal ice zone dynamics: multidisciplinary perspectives and outlooks. *Phil. Trans. R. Soc. A*, 380.

Bouchat, A. and Tremblay, B. (2017). Using sea-ice deformation fields to constrain the mechanical strength parameters of geophysical sea ice. *J. Geophys. Res.*, 122.

Bouillon, S. and Rampal, P. (2015). Presentation of the dynamical core of nextsim, a new sea ice model. *Ocean Model.*, 91.

Boutin, G., Lique, C., Ardhuin, F., Rousset, C., Talandier, C., Accensi, M., and Girard-Ardhuin, F. (2020). Towards a coupled model to investigate wave-sea ice interactions in the arctic marginal ice zone. *Cryosph.*, 14.

Boutin, G., Ólason, E., Rampal, P., Regan, H., Lique, C., Talandier, C., Brodeau, L., and Ricker, R. (2023). Arctic sea ice mass balance in a new coupled ice-ocean model using a brittle rheology framework. *Cryosph.*, 17.

Brouwer, J., Fraser, A. D., Murphy, D. J., Wongpan, P., Alberello, A., Kohout, A., Horvat, C., Wotherspoon, S., Massom, R. A., Cartwright, J., and Williams, G. D. (2022). Altimetric observation of wave attenuation through the antarctic marginal ice zone using icesat-2. *Cryosph.*, 16.

Cavalieri, D. J. and Parkinson, C. L. (2012). Arctic sea ice variability and trends, 1979-2010. *Cryosph.*, 6.

Cheng, S., Stopa, J., Ardhuin, F., and Shen, H. H. (2020). Spectral attenuation of ocean waves in pack ice and its application in calibrating viscoelastic wave-in-ice models. *Cryosph.*, 14.

Chudley, T. R., Christoffersen, P., Doyle, S. H., Abellan, A., and Snooke, N. (2019). High-accuracy uav photogrammetry of ice sheet dynamics with no ground control. *Cryosph.*, 13.

Comiso, J. C., Meier, W. N., and Gersten, R. (2017). Variability and trends in the arctic sea ice cover: Results from different techniques. *J. Geophys. Res.*, 122.

Comiso, J. C., Parkinson, C. L., Gersten, R., and Stock, L. (2008). Accelerated decline in the arctic sea ice cover. *Geophysical Research Letters*, 35.

Cooper, V. T., Roach, L. A., Thomson, J., Brenner, S. D., Smith, M. M., Meylan, M. H., and Bitz, C. M. (2022). Wind waves in sea ice of the western arctic and a global coupled wave-ice model. *Phil. Trans. R. Soc. A*, 380.

Dai, H. J., McWilliams, J. C., and Liang, J. H. (2019). Wave-driven mesoscale currents in a marginal ice zone. *Ocean Model.*, 134.

Dai, M., Shen, H., Hopkins, M. A., and F., A. S. (2004). Waverafting and the equilibrium pancake ice cover thickness. *J. Geophys. Res.*, 109(C07023):81–90.

Day, J. J. and Hodges, K. I. (2018). Growing land-sea temperature contrast and the intensification of arctic cyclones. *Geophys. Res. Lett.*, 45.

DJI (2018). Mavic 2 pro/zoom: User manual.

Doble, M. J., Carolis, G. D., Meylan, M. H., Bidlot, J. R., and Wadhams, P. (2015). Relating wave attenuation to pancake ice thickness, using field measurements and model results. *Geophys. Res. Lett.*, 42.

Dumas-Lefebvre, E. and Dumont, D. (2023). Aerial observations of sea ice breakup by ship waves. *Cryosph.*, 17.

Dumont, D. (2022). Marginal ice zone dynamics: History, definitions and research perspectives. *Phil. Trans. R. Soc. A*, 380.

Dumont, D., Kohout, A., and Bertino, L. (2011). A wave-based model for the marginal ice zone including a floe breaking parameterization. *J. Geophys. Res.*, 116.

Emmanuel, G. V., Rutgersson, A., and Wu, L. (2022). Role of source terms in parameterizing wave decay in the marginal ice zones. *Ocean Model.*, 180.

Feltham, D. L. (2005). Granular flow in the marginal ice zone. *Phil. Trans. R. Soc. A*, 363.

Group, C. D. (1990). Cearex drift experiment. *EOS Trans. Am. Geophys. Union*, 71.

Haas, C., Goebell, S., Hendricks, S., Martin, T., Pfaffling, A., and Saldern, C. V. (2005). Airborne electromagnetic measurements of sea ice thickness : methods and applications. *Arctic*, pages 1–14.

Hakkinen, S. (1987). A constitutive law for sea ice and some applications. *Math. Model.*, 9(2):81–90.

Herman, A. (2022). Granular effects in sea ice rheology in the marginal ice zone. *Phil. Trans. R. Soc. A*, 380.

Hibler, W. (1977). A viscous sea ice law as a stochastic average of plasticity. *J. Geophys. Res.*, 82(27):3932–3938.

Hibler, W. D. (1979). A dynamic thermodynamic sea ice model. *J. Phys. Oceanogr.*, 9.

Hunke, E. C. and Dukowicz, J. K. (1997). An elastic-viscous-plastic model for sea ice dynamics. *J. Phys. Oceanogr.*, 27.

Ip, B., Hibler, W., and Flato, G. (1990). The effect of rheology on seasonal sea ice simulations. *Ann. Glaciol.*, 14.

Johannessen, O. M. (1987). Introduction: Summer marginal ice zone experiments during 1983 and 1984 in fram strait and the greenland sea. *J. Geophys. Res.*, 92.

Johannessen, O. M., Sandven, S., Olaussen, T. I., Johannessen, J. A., Karpuz, R., and Flesche, H. (1990). The pre ers-1 experiments mizex'87 nd sizex'89. *Proceedings of the ninth EARSeL symposium, Espoo, 1989*.

Jop, P., Forterre, Y., and Pouliquen, O. (2006). A constitutive law for dense granular flows. *Nature*, 441.

Khon, V. C., Mokhov, I. I., Pogarskiy, F. A., Babanin, A., Dethloff, K., Rinke, A., and Matthes, H. (2014). Wave heights in the 21st century arctic ocean simulated with a regional climate model. *Geophys. Res. Lett.*, 41.

Kim, Y. H., Min, S. K., Gillett, N. P., Notz, D., and Malinina, E. (2023). Observationally-constrained projections of an ice-free arctic even under a low emission scenario. *Nature Comm.*, 14.

Kohout, A. L., Williams, M. J., Dean, S. M., and Meylan, M. H. (2014). Storm-induced sea-ice breakup and the implications for ice extent. *Nature*, 509.

Kwok, R. (2018). Arctic sea ice thickness, volume, and multiyear ice coverage: Losses and coupled variability (1958-2018). *Env. Res. Lett.*, 13.

Kwok, R., Hunke, E. C., Maslowski, W., Menemenlis, D., and Zhang, J. (2008). Variability of sea ice simulations assessed with rgps kinematics. *J. Geophys. Res.*, 113.

Kwok, R. and Rothrock, D. A. (2009). Decline in arctic sea ice thickness from submarine and icesat records: 1958-2008. *Geophys. Res. Lett.*, 36.

Lemieux, J.-F., Bouillon, S., Dupont, F., Flato, G., Losch, M., Rampal, P., Tremblay, L.-B., Vancoppenolle, M., and Williams, T. (2017). Sea ice physics and modelling. In *Sea Ice Analysis and Forecasting*. Cambridge University Press.

Lemieux, J. F., Knoll, D. A., Tremblay, B., Holland, D. M., and Losch, M. (2012). A comparison of the jacobian-free newton-krylov method and the evp model for solving the sea ice momentum equation with a viscous-plastic formulation: A serial algorithm study. *J. Comput. Phys.*, 231.

Liu, A. K., Holt, B., and Vachon, P. W. (1991). Wave propagation in the marginal ice zone: model predictions and comparisons with buoy and synthetic aperture radar data. *J. Geophys.Res.*, 96:4605–4621.

Longuet-Higgins, M. S. and Stewart, R. W. (1964). Radiation stresses in water waves; a physical discussion, with applications. *Deep-Sea Res.*, 11.

Meier, W., Stroeve, J., Fetterer, F., and Knowles, K. (2005). Reductions in arctic sea ice cover no longer limited to summer. *EOS Trans. Am. Geophys. Union*, 86.

Meier, W. N., Hovelsrud, G. K., Oort, B. E. V., Key, J. R., Kovacs, K. M., Michel, C., Haas, C., Granskog, M. A., Gerland, S., Perovich, D. K., Makshtas, A., and Reist, J. D. (2014). Arctic sea ice in transformation: A review of recent observed changes and impacts on biology and human activity. *Rev. Geophys.*, 52.

NOAA-NCEI (2023). Monthly global climate report for september 2023. Technical report, published online October 2023 retrieved on December 10, 2023 from https://www.ncei.noaa.gov/access/monitoring/monthly-report/global/202309.

NSIDC (September 6, 2012). Arctic sea ice extent settles at record seasonal minimum. Technical report, National Snow and Ice Data Center, http://nsidc.org/arcticseaicenews/2012/09/arctic-sea-ice-extent-settles-at-record-seasonal-minimum/.

Perovich, D., Meier, W., Tschudi, M., Hendricks, S., Petty, A., Divine, D., Farrell, S., Gerland, S., Haas, C., Kaleschke, L., and Pavlova, O. (2021). Arctic report card 2020: Sea ice. *NOAA Arctic Report Card 2020*.

Polyakov, I. V., Walsh, J. E., and Kwok, R. (2012). Recent changes of arctic multiyear sea ice coverage and the likely causes. *Bull. Am. Meteorol. Soc.*, 93.

Rantanen, M., Karpechko, A. Y., Lipponen, A., Nordling, K., Hyvärinen, O., Ruosteenoja, K., Vihma, T., and Laaksonen, A. (2022). The arctic has warmed nearly four times faster than the globe since 1979. *Comm. Earth Environ.*, 3.

Reiner, M. (1945). A mathematical theory of dilatancy. *Am. J. Math.*, 67.

Rivlin, R. (1948). The hydrodynamics of non-newtonian fluids. i. *Proc. R. Soc. A*, 193.

Rottier, P. (1989). Spri participation in the winter marginal ice zone experiment, mizex-87. *Polar Record*, 25.

Sarno, L., Carravetta, A., Tai, Y. C., Martino, R., Papa, M. N., and Kuo, C. Y. (2018). Measuring the velocity fields of granular flows – employment of a multi-pass two-dimensional particle image velocimetry (2d-piv) approach. *Adv. Powder Tech.*, 29.

Saucier, F. J., Roy, F., Gilbert, D., Pellerin, P., and Ritchie, H. (2003). Modeling the formation and circulation processes of water masses and sea ice in the gulf of st. lawrence, canada. *J. Geophys. Res.*, 108.

Serreze, M. C., Holland, M. M., and Stroeve, J. (2007). Perspectives on the arctic's shrinking sea-ice cover. *Science*, 315.

Shen, H. H., Hibler, W. D., and Lepparanta, M. (1987). The role of floe collisions in sea ice rheology. *J. Geophys. Res.*, 92.

Squire, V. (1995). Of ocean waves and sea ice. *Ann. Rev. Fluid Mech.*, 27:115–168.

Squire, V. A. (2007). Of ocean waves and sea-ice revisited. *Cold Reg. Sci. Tech.*, 49.

Squire, V. A. (2018). A fresh look at how ocean waves and sea ice interact. *Phil. Trans. R. Soc. A*, 376.

Squire, V. A. (2020). Ocean wave interactions with sea ice: A reappraisal. *Ann. Rev. Fluid Mech.*, 52.

Squire, V. A. (2022). Marginal ice zone dynamics. *Phil. Trans. R. Soc. A*, 380.

Steele, M., Zhang, J., Rothrock, D., and Stern, H. (1997). The force balance of sea ice in a numerical model of the arctic ocean. *J. Geophys. Res.*, 102.

Stopa, J. E., Ardhuin, F., and Girard-Ardhuin, F. (2016). Wave climate in the arctic 1992-2014: Seasonality and trends. *Cryosph.*, 10.

Stopa, J. E., Sutherland, P., and Ardhuin, F. (2018). Strong and highly variable push of ocean waves on southern ocean sea ice. *Proc. Natl. A. Sci.*, 115.

Stroeve, J., Hamilton, L. C., Bitz, C. M., and Blanchard-Wrigglesworth, E. (2014). Predicting september sea ice: Ensemble skill of the search sea ice outlook 2008-2013. *Geophys. Res. Lett.*, 41.

Strong, C. and Rigor, I. G. (2013). Arctic marginal ice zone trending wider in summer and narrower in winter. *Geophys. Res. Lett.*, 40.

Sutherland, P., Brozena, J., Rogers, W. E., Doble, M., and Wadhams, P. (2018). Airborne remote sensing of wave propagation in the marginal ice zone. *J. Geophys. Res.*, 123.

Sutherland, P. and Dumont, D. (2018). Marginal ice zone thickness and extent due to wave radiation stress. *J. Phys. Oceanogr.*, 48.

Thielicke, W. and Sonntag, R. (2021). Particle image velocimetry for matlab: Accuracy and enhanced algorithms in pivlab. *J. Open Res. Soft.*, 9.

Thielicke, W. and Stamhuis, E. J. (2014). Pivlab – towards user-friendly, affordable and accurate digital particle image velocimetry in matlab. *J. Open Res. Soft.*, 2.

Thomson, J., Lund, B., Hargrove, J., Smith, M. M., Horstmann, J., and MacKinnon, J. A. (2021). Wave-driven flow along a compact marginal ice zone. *Geophys. Res. Lett.*, 48(3):e2020GL090735.

Thomson, J. and Rogers, W. E. (2014). Swell and sea in the emerging arctic ocean. *Geophys. Res. Lett.*, 41.

Tietsche, S., Day, J. J., Guemas, V., Hurlin, W. J., Keeley, S. P., Matei, D., Msadek, R., Collins, M., and Hawkins, E. (2014). Seasonal to interannual arctic sea ice predictability in current global climate models. *Geophys. Res. Lett.*, 41.

Tremblay, L. B. and Hakakian, M. (2006). Estimating the sea ice compressive strength from satellite-derived sea ice drift and ncep reanalysis data. *J. Phys. Oceanogr.*, 36.

Uzuner, M. S. and Kennedy, J. F. (1976). Theoretical model of river ice jams. *ASCE J. Hydraul. Div.*, 102.

Vichi, M. (2021). A statistical definition of the antarctic marginal ice zone. *Cryosph.*

Wadhams, P., Squire, V. A., Ewing, J. A., and Pascal, R. W. (1986). The effect of the marginal ice zone on the directional wave spectrum of the ocean. *J. Phys. Oceanogr.*, 16.

Webber, J. E. (1987). Wave attenuation and wave drift in the marginal ice zone. *J. Phys. Oceanogr.*, 17.

WMO (2014). World meteorological organization. sea ice nomenclature no. 259, volume i - terminology and codes.

Yamamoto, F. and Ishikawa, M. (2022). A review of the recent piv studies from the basics to the hybridization with cfd. *J. Flow Control Measur. Vis.*, 10.

Zhang, Y. and Hunke, E. C. (2001). Recent arctic change simulated with a coupled ice-ocean model. *J. Geophys. Res.*, 106.